CHAPTER III

THERMOCAPILLARY INTERACTION OF TWO BUBBLES OR DROPS

3.1 Introduction

In this chapter, we study the interactions between a pair of bubbles or drops, using both two- and three-dimensional simulations. Before discussing these simulations, a convergence test on a single bubble is done, followed by a study of the effect of the various governing parameters on the migration velocity and the deformation of a single bubble. While most of these effects are already known, we nevertheless report them here to gain insight and to prepare the reader for the discussion of more complex results, such as the two-bubble and the multi-bubble simulations. To understand the behavior of a bubble cloud, it is essential to know the basic mechanisms acting between a few bubbles. The two-bubble interaction is the simplest case and has attracted considerable attention in the past as a result.

3.2 Resolution test

Here, we do a resolution test in the region where the non-dimensional numbers are high. We have computed the migration velocity of a single bubble until it reaches a steady state. We have explored the sensitivity of the solution to the grid resolution

by simulating a single bubble on a 32×64, 64×128 and 128×256 grid for a domain which extends 4 bubble radii in the x direction and 8 bubble radii in the z direction. This corresponds to 16, 32 and 64 grid points per bubble, respectively. The non-dimensional numbers for this resolution test are: $Re = 5, Ma = 20, Ca = 0.01666$, while the ratio of the physical properties is 0.5 Figure 3.1 shows the velocity field in the top row, isotherms in the middle row and streamlines in a frame moving with the bubble in the bottom row. The resolution increases from left to right. Careful inspection of the last two columns indicates that the differences between these are small. As seen in Figure 3.2(a) and Figure 3.2(b), as the resolution is increased, the terminal velocities and the trajectories converge and we observed that beyond the 64×128 grid the change is negligible, amounts to about 0.6%. The difference between 16 grid points per bubble and 32 grid points per bubble resolution is about 2.1%. Therefore, the 32 grid points per bubble resolution was chosen for most of the simulations presented here in order to save computational resources. Where only qualitative information is required, we can use as few as 16 grid points per bubble, with an error of approximately 3%.

3.3 Thermocapillary migration of a single bubble

Here, we examine the effect of the various controlling parameters on the motion of a single bubble, specifically the rise velocity and the deformation.

To show the effect of the various non-dimensional parameters, the temperature and stream function contours for several different Marangoni numbers are plotted in Figure 3.3. The Marangoni numbers for each column, from left to right, are $1, 10, 20, 40$, and 60. The Reynolds number, $Re = 1$, and the Capillary number, $Ca = 0.0666$, for all these calculations. The ratio of the physical properties, bubble

to host fluid, is 0.5. The size of the domain in the horizontal direction is 5 times the bubble radius and the vertical size of the domain is 10 times the bubble radius. Here, we plot the stream function contours in a laboratory fixed frame since the contours in a frame which is moving with the bubble do not show any interesting behavior. In all frames, the bubble has reached an essentially steady state. The major difference is the shape of the temperature contours and the structure of the wake. As the bubbles rise they carry cold fluid from the bottom. This fluid heats up as the bubble moves into warmer fluid and the disturbance in the temperature contours is a reflection of the relative importance of advection over conduction. The disturbance is smallest for the low Marangoni number computation on the left and largest for the high Marangoni number computation on the right. Although the wake is similar in the four last frames, the stagnation point is further away from the bubble in the run on the left. Although we plot 20 equally spaced streamlines close to the bubble, two more streamlines have been added in order to capture the wake region below the dividing streamline. In the first frame, no dividing streamline exists since the Marangoni number in this case is small enough. As a result, convection of energy is negligible and the rise of the bubble is similar to a bubble rising in an unbounded domain, where no dividing streamline exists in the creeping flow regime. The streamlines shown here are nearly identical to those found by Subramanian (1992) for axisymmetric bubbles. Figure 3.4(a) shows the migration velocity versus time. As we increase the Marangoni number, the migration velocity decreases. As a consequence of an increase in the convective transport of energy, the isotherms wrap around the bubble and this causes a reduction in the thermocapillary driving force and hence migration velocity. The bubble remains nearly cylindrical for the computations shown here. Figure 3.4(b) shows that the deformation is decreasing

with increasing Marangoni number. However, the magnitude of the deformation is very small. Since the temperature distribution around the bubble is more uniform for higher Marangoni numbers, the change in thermocapillary driving force around the bubble is small. This results in a small deformation of the bubble. Although we terminate these computations before the bubble reaches the top of the domain, we have conducted other calculations where the bubble interacts with the wall and have observed deformations similar to those computed by Ascoli and Leal (1990).

To show the effect of the Reynolds number, we present, in Figure 3.5, the temperature and stream function contours for three different cases. The Reynolds number for each column, from left to right, is $1, 5$, and 10. The Marangoni number, Ma, is 1 and the Capillary number and the ratios of the physical properties are the same as in the previous case. In all three frames, the bubble has reached steady state. Since the Marangoni number is unity, the conduction and convection of energy are equal. As a result, the isotherms are identical. The major difference is the structure of the wake. The streamlines in the high Reynolds number run on the right show that the stagnation point is close to the bubble compared to the run in the middle frame. As in the previous case, two more streamlines are added in order to capture the wake region below the dividing streamline. The first column is the same as the first column in the previous case and was discussed there. The bubble remains nearly cylindrical in this case, as well. The migration velocity decreases with increasing Reynolds number as seen in Figure 3.6(a) although the reduction is small. An inspection of Figure 3.6(b) indicates that the bubble deforms much more, compared to the previous variable Marangoni case in Figure 3.3. This is an interesting result since previous results in the literature indicate that the migration velocity of a bubble increases with increasing Reynolds number for spherical shape bubbles. Therefore, the assumption of a

non-deformable bubble is not valid and can cause unphysical predictions. It is the deformed shape of the bubble that leads to a reduction in the migration velocity.

The effect of the Capillary number on the migration velocity and the deformation of the bubble is plotted in Figure 3.7(a) and (b). For these different Capillary number runs, the other non-dimensional numbers are: Reynolds number, $Re = 1$; Marangoni number, $Ma = 10$; and $\mu^* = k^* = \rho^* = {c_p}^* = 0.5$. As noted earlier, zero Capillary number corresponds to a spherical bubble and as the Capillary number increases, the deformation of the bubble increases, as well. Figure 3.7(b) shows that this is indeed the case although the magnitude of the deformation is not big. Figure 3.7(a) shows that the migration velocity of the bubble decreases with increasing Capillary number. This is consistent with the results of Chen and Lee (1992) who also reach similar conclusions.

When the viscosity of the ambient fluid is lower than the bubble viscosity, the viscous shear stresses in the ambient fluid are smaller and most of the work of surface tension forces is done on the fluid inside the bubble. As a result, less fluid flows down around the bubble. Since the motion of the bubble is a reaction to the motion of the ambient fluid, the bubble will migrate with a smaller migration velocity. Figure 3.8(a) shows this behavior clearly. As the viscosity ratio increases, the migration velocity decreases. Here, the other non-dimensional numbers are, $Re = 1$, $Ma = 10$, $Ca = 0.0666$ and $k^* = \rho^* = c_p^* = 0.5$.

Figure 3.8(b) shows the effect of the ratio of the heat conductivity coefficients on the migration velocity. The migration velocity of the bubble is higher when the temperature gradient across the bubble is high. As a bubble in a temperature gradient moves toward the hot region, the north pole of the bubble absorbs heat and the south pole gives off heat to the cold ambient fluid. When the heat conductivity

of the bubble is negligible, heat cannot enter at north pole of the bubble, nor leave to the ambient fluid at the south pole. This results in a temperature field where the isotherms are perpendicular to the bubble surface, showing no heat transfer to the bubble. As a result, the temperature gradient across the bubble's south and north poles is high, and consequently the migration velocity is high. Here the non-dimensional numbers are, $Re = 1$, $Ma = 10$, $Ca = 0.0666$ and $\mu^* = \rho^* = c_p^* = 0.5$.

Since the density of a drop is higher than that of the ambient fluid it should be expected that the drop will accelerate more slowly than a gas bubble. Figure 3.9(a) shows this slower acceleration when the density ratio is 10. Furthermore, with increasing density of the bubble phase, the heat convection inside the drop will increase. The isotherms will be more curved toward the hot portion of the drop surface. Because of this, a more uniform temperature field will be present inside the drop. Consequently, the migration velocity of the drop decreases with increasing drop density. This behavior is seen in Figure 3.9(a). The same argument also holds for the heat capacity ratio. The reduction of the drop migration velocity with increasing heat capacity is shown in Figure 3.9(b). Here the non-dimensional numbers are, $Re = 1$, $Ma = 10$, $Ca = 0.0666$ and for the density ratio effect $\mu^* = k^* = c_p^* = 0.5$ and for the heat capacity $\mu^* = \rho^* = k^* = 0.5$.

3.4 Effect of initial position on the interaction of two bubbles

After obtaining some insight about the thermocapillary migration of a single bubble, we move to the interaction of two bubbles. To understand the effect of the initial orientation of the bubbles on the evolution, we vary the gap between the bubbles and their angular position with respect to the initial temperature gradient. In Figure 3.10(a), (b) and (c), the angle between the x axis and a line connecting the

center of the bubbles is $\pi/8, \pi/4$ and $3\pi/8$, respectively. The angular orientation of the bubbles in the other frames, $(d), (e), (f)$ is the same. In the first three frames, the gap between the bubbles, center to center, is 2.5 times the bubble radius. In the last three frames, this distance is three bubble radii. The computations was done on a domain which is 8 bubble radii wide in x and 16 bubble radii high in z. The resolution used here is 128×256 grid points. The non-dimensional numbers for all the cases are: $Re = 10, Ma = 10, Ca = 0.041666$ while the ratio of the physical properties is equal to 0.5.

We report the results of these simulations in Figure 3.11 and Figure 3.12. An inspection of Figure 3.11(a) and (b) shows that the bubbles close the gap between themselves in the vertical direction while placing themselves side by side, almost equispaced across the channel. The last case is, however, an exception. Since the gap is large and the bubbles are almost oriented in tandem in that case, it takes a larger distance to close the gap vertically and the bubbles reach to the top wall before lining up across the channel. Nevertheless, the trends suggest that they will behave similar to the other cases, if given a longer box. Figure 3.12 shows the migration velocity difference between the bubble on the right and the bubble on left. This figure also shows that as the bubbles migrate in the vertical direction, they catch up with each other. When the bubbles reach a steady state, they migrate with the same velocity, side by side.

3.5 Two dimensional simulations of two bubbles or drops

While the primary goal of this study is to understand the basic physics involving bubble pairs in a real physical situation, much information can be gained by two dimensional simulations, even though they must be regarded as only a step toward fully

three dimensional simulations. In this section, we discuss the interactions between two-dimensional bubbles and drops.

First, we explore the motion of gas bubbles. The physical properties of a gas bubble are small compared to the ambient fluid. Thus, the viscosity, the density, the coefficients of heat conductivity and the heat capacity are much smaller in the gas than in the fluid phase. In view of the findings of Chapter II, and the earlier sections of this chapter, where we examined the effect of the physical parameters on the bubble's migration velocity, we choose the ratio of physical properties to be $1/25$, which is low enough to simulate the motion of a gas bubble. We take the Capillary number as fixed at $Ca = 0.04166$ in all simulations done in this section, but use various Reynolds and Marangoni numbers. The resolution for these runs is 128×256 grid points and the computational domain is 8 bubble radii wide in x and 16 bubble radii high in the z direction. The bubbles are released close to each other and the bubble on the right is ahead of the other bubble initially. The bubble on the left is at $x/a = 2.9$ and $z/a = 4$, and the one on the right is at $x/a = 5.1$ and $z/a = 5.8$. Here, both the Reynolds and the Marangoni numbers are 40; therefore convective transport of energy and momentum are higher than viscous and thermal diffusion. Figure 3.13 shows the velocity field, and the corresponding isotherms are plotted in Figure 3.14 at different times, showing the evolution.

As the bubbles rise, the bubble on the left first catches up with the bubble on the right. It draws hot fluid down its side and as the bubble on the right rises, some of this fluid is drawn into its wake, thereby reducing slightly the temperature increase across the bubble on the right and hence its velocity. After the bubbles move slightly closer together, the fluid in the narrow gap between the bubbles is pushed down more than in the wider gap, since the contribution of each bubble to

the velocity field adds in this region. This is seen in the second frame of the velocity field. Hence, more hot fluid is drawn into the narrow gap between the bubbles than into the wide one. As a result, the bubbles attract each other. After they collide, they bounce back and the bubble on the left pushes the bubble on the right to the right. Since it catches up with a large velocity, it hits the bubble on the right and causes it to rotate clockwise. As seen in Figure 3.15(a), the bubble on the left has a higher migration velocity. After the collision, this bubble still moves faster upward than the other one and the bubble on the right is caught in the wake of the left one which is now ahead of it. Because of this, we see an interesting phenomena here, as well as in Figure 3.16; namely, that the bubble being caught in the wake of the other one migrates against the temperature gradient. From the temperature field in Figure 3.14, it is seen that when the bubbles are close, the hot ambient fluid flows down in the wide gap, satisfying the conservation of mass. Since the bubbles migrate toward the hot region, the bubbles move apart. This is seen in the fourth frame of Figure 3.14. Later, the bubble on the right moves far away from the bubble on the left and crosses into the next periodic box while still accelerating to reach its steady state migration velocity. Since the boundary conditions are periodic in x, we see the bubble reentering from the left side of the computational box. This time the bubbles collide horizontally and bounce back. The collision is not as strong as the previous one, as is seen from the trajectories in Figure 3.16. After the second collision, the bubbles move away from each other and migrate toward the hot wall. We have stopped the simulation before the bubbles hit the wall. If the periodic box is wide enough, it can be easily concluded that after the first collision, the bubbles would separate and migrate toward the hot wall almost independent of each other, similar to a single bubble migration. It should also be noted that the temperature

field is disturbed much more by the circulating flow in the wake region of the bubbles than in the field ahead of them.

In the last frame of Figure 3.14, the temperature gradient across each bubble clearly shows its direction of motion. Figure 3.15(d) shows that the bubbles, by closing the gap in vertical direction, eventually move side by side. The internal circulation plot in Figure 3.15(b) indicates that the direction of motion of the bubbles is consistent with the sign of the internal circulation. From the elementary theory of lift, the bubble would move to the left in the configuration presented when the internal circulation is positive and it is in a uniform incoming velocity field. The internal circulation is calculated by $\oint \mathbf{u}_s \cdot d\mathbf{s}$ along the interface. When the bubbles collide, Figure 3.15(c) shows that the deformation increases with each collision.

We have repeated these computations for various Re and Ma numbers and studied the effect of these numbers on the separation distance and the migration velocity difference between the bubbles. We show these quantities in Figure 3.17. Although we attempted to simulate the $Re = 60, Ma = 20$ case, this was not possible because the pressure solution did not converge. The different Re and Ma number cases in Figure 3.17 indicate that the vertical alignment of the bubbles is unstable and bubbles eventually come side by side to form a more stable layer. When the bubbles migrate, they overtake each other but eventually the oscillation in the vertical gap dies out. The bubbles try to space themselves equally across the channel (note that the computational box is periodic in horizontal direction). The first case, $Re = 10, Ma = 10$ exhibits different behavior from the rest. In this case, the bubbles close the vertical gap much faster and reach to the same migration velocity in a shorter time. The most significant difference is seen in the horizontal spacing of the bubbles in Figure 3.17. The bubbles come side by side, migrate together for a

long time and move apart only very slightly, retaining the initial separation. It is likely that these bubbles would coalescence if the interface were allowed to rupture but here we do not allow that to happen.

We then move to the interactions of two drops. The density of a drop is higher than that of the ambient fluid and we choose a density ratio of 10. Other ratios of the physical properties are the same as for the gas bubbles, namely $\mu^* = k^* = c_p^* = 1/25$. The Capillary number, the resolution, as well as the computational domain size are also the same as in the previous case. The drops are released close to each other with an arbitrary orientation with respect to the temperature gradient. The initial positions of the drops are the same as in the previous case in Figure 3.13. We also do these simulations for various Reynolds and Marangoni numbers. Similar to the gas bubbles, we report one of these cases where both the Reynolds and the Marangoni numbers are 40.

Figure 3.18 and Figure 3.19 show the velocity field and the isotherms, respectively, at different times. Some differences are easily seen in the interaction of drops as compared with the gas bubbles. Inspection of the velocity field shows that the interaction takes place from the beginning to the end in the computational box considered. The drops, also, do not cross the periodic boundaries. The velocity field plot shows strong velocities inside and outside of the drops. Especially, strong recirculating zones in the wake of the drops at later times are visible. It is also seen that the drops deform much more than the gas bubbles. The deformation occurs in such a way that the drops elongate in the flow direction. The isotherms show another major difference, inside the drops. Due to the convective transport of energy inside the drops, the temperature field inside the drops is very contorted. The isotherms wrap along the inside surface of the drop, causing it to slow down. The high velocity

in the wake of the drops disturbs the temperature field considerably in this region. While the thermal wake region extends all the way to the bottom wall, the velocity and temperature field ahead of the drops remain almost unaffected due to small effect of conduction.

As seen in the velocity and the isotherm plots, the hot ambient fluid flows through the narrow gap between the drops, since each drop pushes the ambient fluid in the same direction in this region. As a result of this behavior, the drops move closer to each other. Similar behavior is also seen in the trajectories in Figure 3.21. When the drops collide, the drop on the left bounces back and slows down. This collision causes the drop on the right to speed up sharply, although it was initially moving slower than the drop on the left. The drop on the left feels the effect of the impact and slows down quickly. After the collision, both drops accelerate and migrate upward as seen in frames four to six of the velocity field. However, the drop on the left accelerates faster and catches up with the other drop in the sixth frame. Until then, unlike the interactions between gas bubbles, the drops do not come side by side, but migrate to a position such that the drop on the right is ahead of the drop on the left, but slightly on the left side, similar to their initial position. This is the major difference between the behavior of drops and the gas bubbles. Right before hitting the upper wall, the drops collide once more. The collision at this time is weak, causing small acceleration of the drop on the right and deceleration of the drop on the left. In the last time frame of the plot of the temperature field, since the drop on the right is very close to the wall, the drop on the left slides to the left so that it reaches the upper wall. Figure 3.20 shows a more quantitative description of this simulation where the migration velocity, internal circulation, deformation and separation distance are plotted. After each collision, the change in internal circulation and deformation is

obvious. The vertical and the horizontal separation distance between the drops is clear in Figure 3.20(d). Although the vertical distance decreases in the early stages of the interaction, where the drops attract each other, later on this gap increases, showing the trend explained above. Because of this orientation of the drops, the horizontal gap obviously get smaller.

We have done simulations of drops for various Re and Ma numbers and have studied the effect of these numbers on the vertical and horizontal separation distance between them as a function of time. We show these quantities in Figure 3.22. The different Re and Ma number cases in Figure 3.22 clearly show that the behavior seen in the gas bubbles simulations does not apply to drops. When $Re = 60$ and $Ma = 20$, it seen that the drops close the vertical gap and move away from each other in the horizontal direction. Since they separate in the horizontal direction, their influence on each other becomes minimal. The other cases behave differently. When the Reynolds and the Marangoni numbers increase equally, there is a transient behavior seen in that plot. When both Re and Ma are 10, the drop on the left takes over and moves ahead of the drop on the right in the late stages of the simulations. The drops also separate horizontally. When Re and Ma are increased to 20, the drop on the left catches up with the drop on the right, but eventually the drop on the left takes over, just before both drops hit the top wall. They also separate horizontally but less than in the previous case. Further increase of Re and Ma to 40 shows a different picture. The drop on the right always stays ahead of the other drop and, most importantly, the vertical gap between them increases while the horizontal gap decreases. This is the case that we discussed earlier. In the final case, where Re and Ma are increased to 60, this behavior continues. This time, the drop on the right is well ahead of the other one while the horizontal gap is reduced significantly and

these drops are almost in tandem when they reach the upper wall.

Next, we examine an intermediate case with bubbles where the physical properties of the bubble phase are half those of the ambient fluid. We also conduct these simulations for different Re and Ma numbers. The Capillary number, the initial position of the bubbles, the domain size and the resolution is the same as for the gas bubbles case in Figures 3.13 - 3.16. The velocity field, Figure 3.23, is similar to the velocity field of the gas bubbles in Figure 3.13, showing the recirculation zones in the wake of the bubbles. Figure 3.24 shows the temperature contours at different times. As the bubbles rise, the bubble on the left first catches up with the bubble on the right. As seen for the gas bubbles, it draws hot fluid down its side and as the bubble on the right rises, some of this fluid is drawn into its wake, thereby reducing slightly the temperature increase across it and hence its velocity. While the bubbles are moving side by side, close to each other, they migrate like one big bubble. Since the ambient fluid can no longer flow between them, it flows down near the side of the periodic box. Bubbles move toward the hot regions and separate as they continue to migrate to the upper wall. Since the bubble on the left pushes the bubble on the right to the side, and also due to the temperature gradient, the bubble on the right slides to the side, reappearing from the left side of the periodic box. From then on, the bubbles migrate side by side, almost equispaced across the channel. This is due to the fact that once the bubbles are side by side, and moving upward, the outer fluid has to flow down between them to satisfy continuity and when the spacing between the bubbles is uneven there is greater flow through the larger spacings. Since the downward moving fluid is hotter, the isotherms are pushed farther down where there is a large space between the bubbles than when the space is small. This is very clear in the second frame. Since the bubbles move from colder parts of the domain to the

hotter ones, this leads to a lateral motion (in addition to the upward motion) where the small spaces become larger and the large spaces become smaller until the bubbles have arranged themselves in a horizontal array with equal spaces between them.

Figure 3.25 shows the migration velocity, the internal circulation, the deformation and the separation distance for the run in Figures 3.23 and 3.23. The initial acceleration is similar to the one bubble case, both bubbles accelerate rapidly, reach a large velocity and then slow down. The bubble on the left, that is closer to the bottom of the box, reaches a higher initial velocity and slows down more slowly than the one on the right. It is seen from this plot that the bubble on the left migrates at an almost steady state velocity in the last half of the interaction process. The deformation decreases in that period, too. The trajectories of the bubbles are plotted in Figure 3.26.

Investigations for different Re and Ma numbers shown in Figure 3.27 exhibit similar behavior as the gas bubbles considered in Figure 3.13. In all cases the bubbles close the vertical gap between them. As the non-dimensional numbers increase, the interaction becomes stronger and the bubble on the right crosses over to the next periodic box. Since the system is periodic horizontally, the bubble reenters through the other side of the box. Therefore, while the horizontal separation is calculated between the bubble on the right and the bubble on the left, it should actually be measured between the bubble on the left and the bubble which reenters from the left side of the domain once the one on the right crosses to the next periodic box. Thus, the results in Figure 3.27(b) show that two bubbles space themselves across the channel as equispaced as they can.

We have also investigated another case where the density and the heat capacity ratio of the bubble phase is half that of ambient fluid, but viscosity and heat

conductivity ratio is 1/25, similar to Figure 3.13. Although we also explored several Reynolds and Marangoni numbers, the only qualitative difference we found is the structure of the temperature field inside the bubbles. The convection of energy inside the bubble is high and the isotherms are similar to the isotherms inside the drops while the temperature field in the ambient fluid is not much different from Figure 3.24.

3.6 Three-dimensional simulations of two bubbles

After gaining some insight into the interactions of two bubbles from two-dimensional simulations, we explore the interaction of two bubbles by fully three-dimensional simulations in this section.

The ratios of the physical properties are 0.5, same as for the two dimensional cases discussed at the end of Section 3.5. The Capillary number is also the same. The resolution for these runs is $64 \times 32 \times 128$ grid points in a $x/a = 5.71$, $y/a = 2.86$, $z/a = 11.43$ computational box. The bubbles are close to each other and are perturbed so that the bubble on the right is ahead of the other one. The location of the left bubble is $x_l/a = 1.71$, $z_l/a = 2.85$ and that of the right bubble is $x_r/a = 4$, $z_r/a = 3.43$. They are placed in the middle cross sectional plane in the y direction. The thermal gradient is such that temperature increases toward the top hot wall.

We report two different cases. For the first one, $Re = 20$ and $Ma = 60$. The bubbles are shown in Figure 3.28, along with the velocity and the temperature field in the middle cross sectional plane. A more detail description of the velocity field and isotherms in that plane are plotted at different times in Figure 3.29 and Figure 3.30, respectively. The first frame in Figure 3.28 shows the starting motion of the bubbles where the velocity field is weak. In the second frame the velocity is much

stronger than in the other frames. This is the time when the bubbles attain their highest migration velocity. The interaction follows a similar pattern as was seen in the two dimensional simulations. Since the ambient fluid between the bubbles is pushed down, as is seen from the velocity field, the bubble on the left is attracted to the bubble on the right. The curved isotherms in Figure 3.30 show the relative effect of the convective transport of energy. Since the Marangoni number is high, the convection of energy is large. Both bubbles accelerate very fast, attain a high migration velocity and then slow down. When the bubble on the left moves to the right, it pushes the other bubble to the side. As the bubbles get close to each other, the hot ambient fluid flows down along the sides of the computational box, thereby increasing the temperature in that region. This is clearly seen in the third frame of the isotherms in Figure 3.30. This shape of the isotherms is also determined by the fact that the bubbles carry cold fluid with them. As a result, they move apart. Since the bubble on the left has a higher velocity, it catches up with the other one. As they slow down to a steady migration velocity, the velocity difference between them decreases, as is seen in Figure 3.31(d). Figure 3.31 gives a more quantitative description of this simulation. The migration velocity, vertical position, separation distance, and velocity difference are plotted versus time. Figure 3.31 as well as Figure 3.32, where the trajectories are shown, show that when the bubbles reach a steady state, they are almost side by side and equispaced horizontally. The behavior of the bubbles presented here confirms the predictions of the two-dimensional simulations discussed in Section 3.5.

Comparison of two- and three-dimensional simulations reveals that the disturbances of the velocity and the temperature field decay in the three-dimensional simulations at a much faster rate than in the two dimensional simulations as we go

away from the bubbles. See, for example, the isotherms in Figure 3.30. Although weak, recirculating zones seen in two-dimensional simulations are also observed in the three-dimensional simulations and are visible in the middle frames of the velocity field.

After examining the interactions between two bubbles in a parameter range where convective transport of energy is higher than convective transport of momentum, we move to the second case where $Re = 60$ and $Ma = 20$. All other parameters are the same as in the previous case. Here, we place the bubbles in such a way that they are disturbed more in the vertical direction than in the previous case. Specifically, the left bubble is at $x_l/a = 2.14$ and $z_l/a = 2$ and the right bubble is at $x_r/a = 3.57$ and $z_r/a = 3.85$. Both are placed in the middle cross sectional plane in the y direction. Figure 3.33 shows the evolution of this case. Both the velocity field and the temperature field are plotted in the middle cross sectional plane. The velocity field in that plane is also while in Figure 3.34 and Figure 3.35 shows the isotherms in the same plane. It is easily seen that there are some differences in the velocity field compared with the previous case. Although the first frame of both Figure 3.28 and Figure 3.33 are similar, the rest of the evolution is different and the velocity does not decrease here. An inspection of Figure 3.36, where a more quantitative description of this simulation is presented, shows that although the bubbles slow down, the rate of decrease is small. After reaching an initial high velocity, they migrate at this high velocity until they reach the upper wall. Although the velocity decreases slightly at the end of the simulations, the bubbles do not have enough distance to slow down to a steady migration velocity. This behavior is due to the higher Reynolds number and is similar to what was seen in the two-dimensional, two-bubble interaction. Nevertheless, Figure 3.36 shows that as in the previous case,

the bubbles strive to close the vertical gap while moving apart in the horizontal direction. From the trajectories in Figure 3.37 it is seen that the bubble on the left is ahead and moves straight up while the other one slides to the side. This is due to the temperature field which is different than the previous case, see Figure 3.37. The bubble on the left does not feel the effect of the other bubble to any significant degree. But, since the bubble on the left migrates straight ahead faster, it pushes the other bubble to the side which is actually blocking the way of the other bubble. The forth and the fifth frames of Figure 3.35 show that the ambient fluid on the right side of the bubble on the right is hotter than on the other side. Therefore, the bubble should move to the right as it does, because bubbles move in the direction of a higher temperature.

Since the convective transport of energy is not as high as in the previous case, the isotherms do not curve as much. While the disturbances of the temperature field decay as fast as the previous case, the velocity fields differ. Once the recirculation zones form, they are present until the end of the simulation, as seen in Figure 3.34.

We have also computed similar simulations for different Reynolds and Marangoni numbers. Figure 3.38, where the vertical and the horizontal separation distance between the bubbles are shown, summarizes the results of these simulations. In all these different Re and Ma number cases, it is seen that the bubbles strive to close the vertical gap while moving apart horizontally.

3.7 Conclusion

The major finding reported here is the tendency of the bubbles to line up, side by side, perpendicular to the temperature gradient. While this behavior appears to be similar to what is found for spheres and cylinders in fluidized beds, where rows

of spheres align themselves into a string perpendicular to the flow, the mechanism here is different. For solid spheres the reason is the low pressure region at the "waist" which attracts other particles. In the simulations carried out here the bubbles actually repel each other, since cold fluid is more easily carried with the bubbles in the narrow gaps between them than in bigger gaps, and the bubbles generally move away from cold regions. Thus, while the bubbles line up across the channel they tend to maximize the distance between adjacent bubbles. This formation of bubble layers could be of considerable significance for material processing in microgravity where layers like these might affect the bulk properties of solidified material. Drops, on the other hand, behave somewhat differently. In the low Re and Ma number region they behave similar to bubbles, but they tend to line up in tandem in most of the simulations presented here when both Re and Ma are high. Drops also deform much more than bubbles along the direction of the temperature gradient.

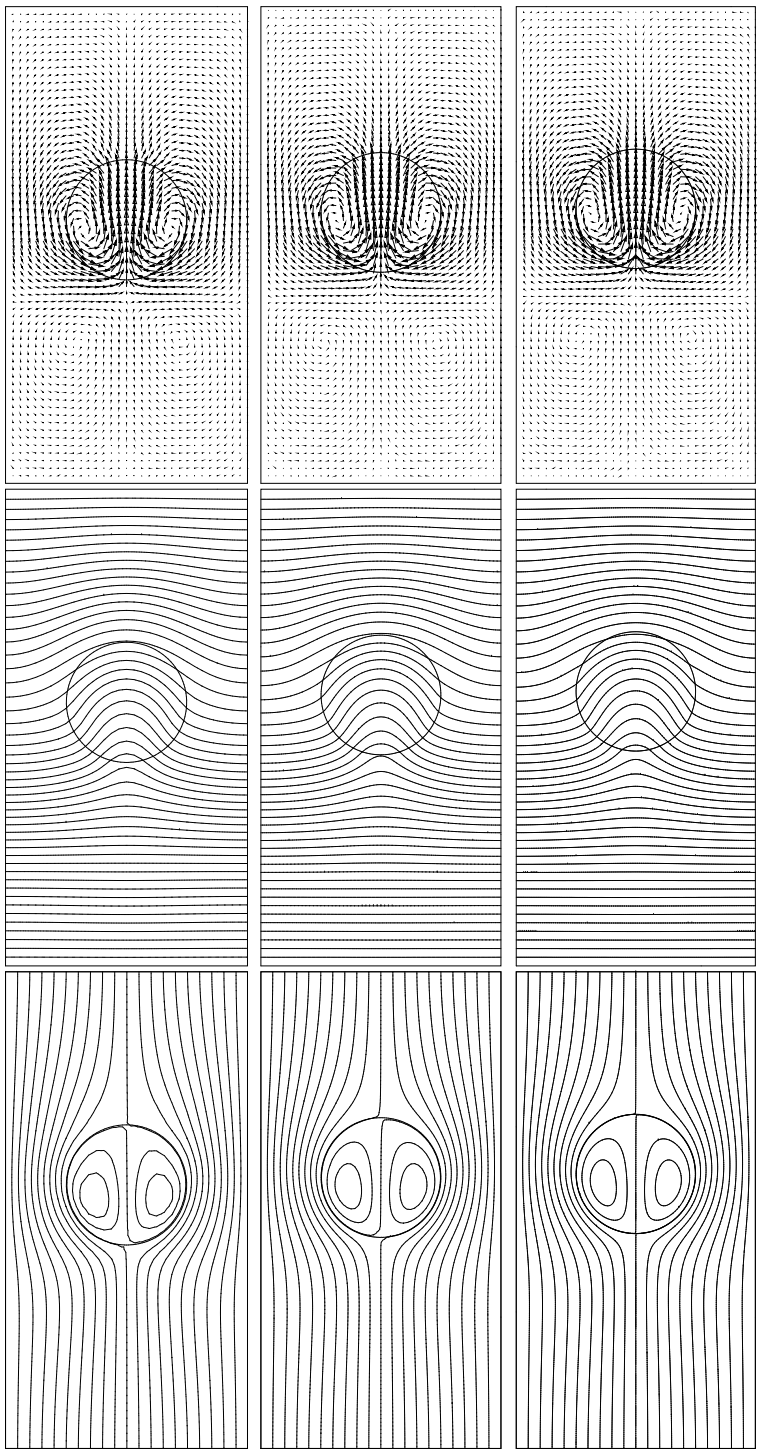

Figure 3.1: Velocity field (top), isotherms (middle) and streamlines (bottom) of a single bubble rising at steady state. 32×64 grid points of the velocity field, 50 equally spaced isotherms and 21 equally spaced streamlines in a frame moving with the bubble are shown. First column is a 32×64 grid, second column is for a 64×128 grid and third column is for a 128×256 grid.

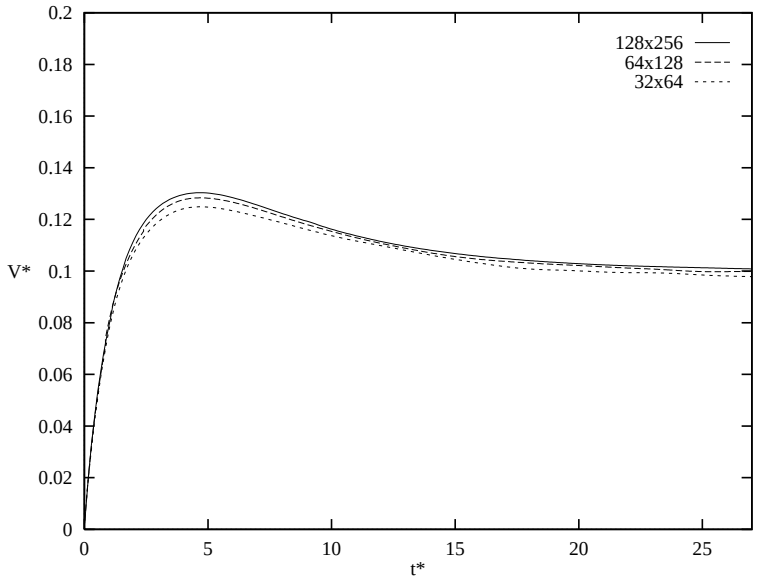

(a) Migration velocity

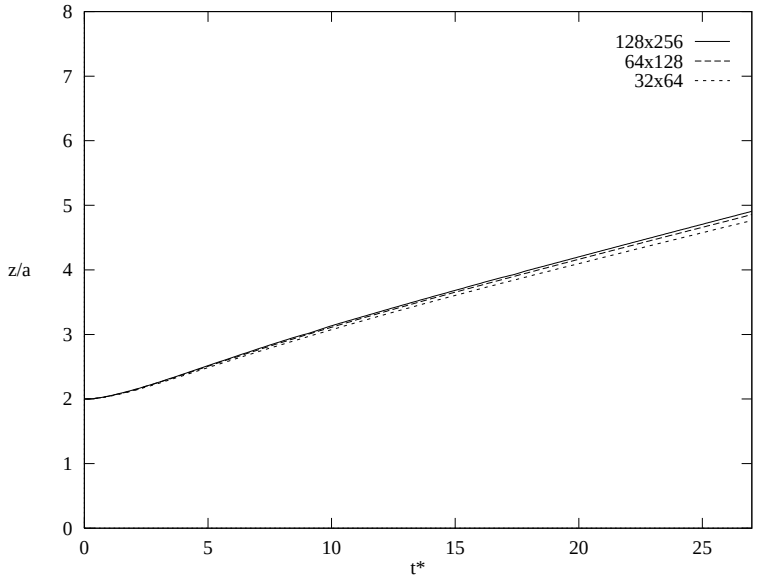

(b) Trajectories

Figure 3.2: Resolution test for a single bubble. (a) Migration velocity versus time (b) z component of the trajectories versus time.

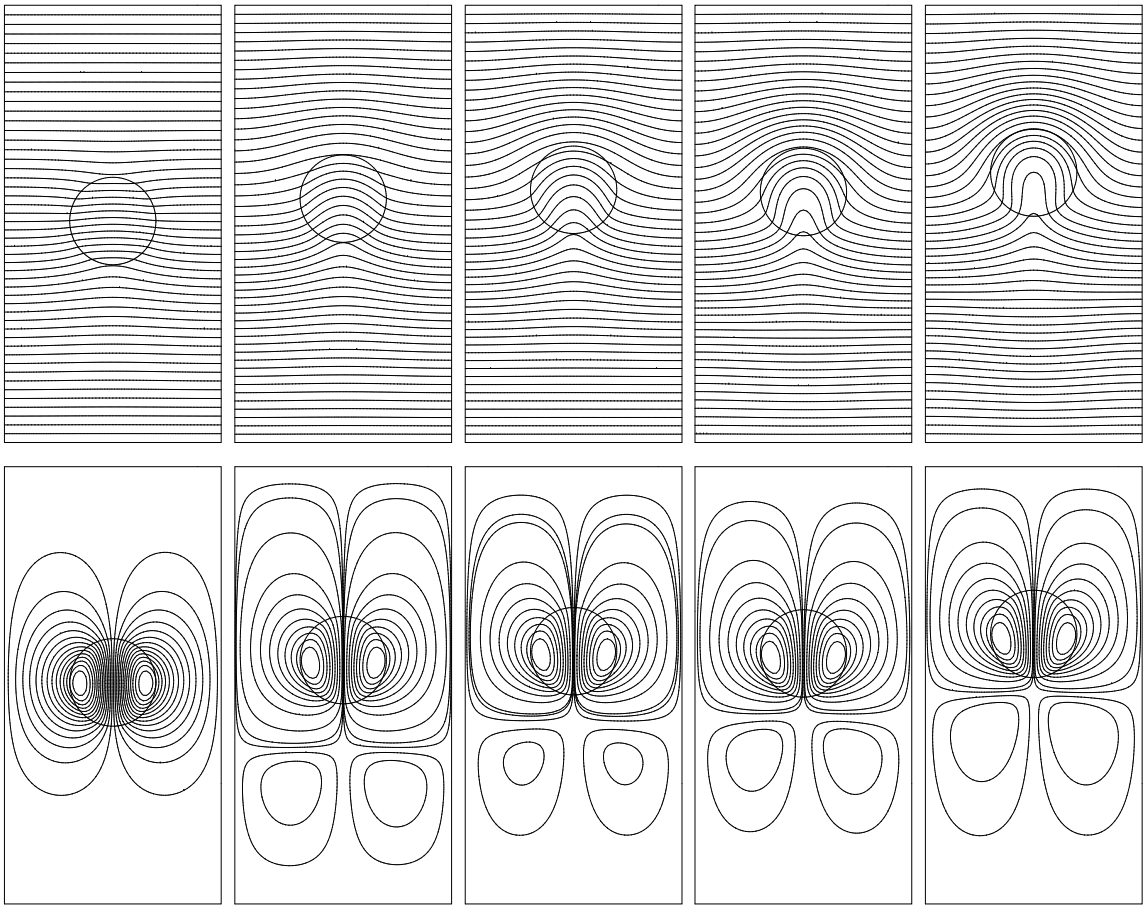

Figure 3.3: Isotherms (top) and streamlines (bottom) of a single bubble migrating at steady state for different Marangoni number. 50 equally spaced isotherms and 20 equally spaced streamlines are shown. Marangoni number for each column from left to right is 1, 10, 20, 40, 60. Here, $Re = 1$ and $Ca = 0.06666$.

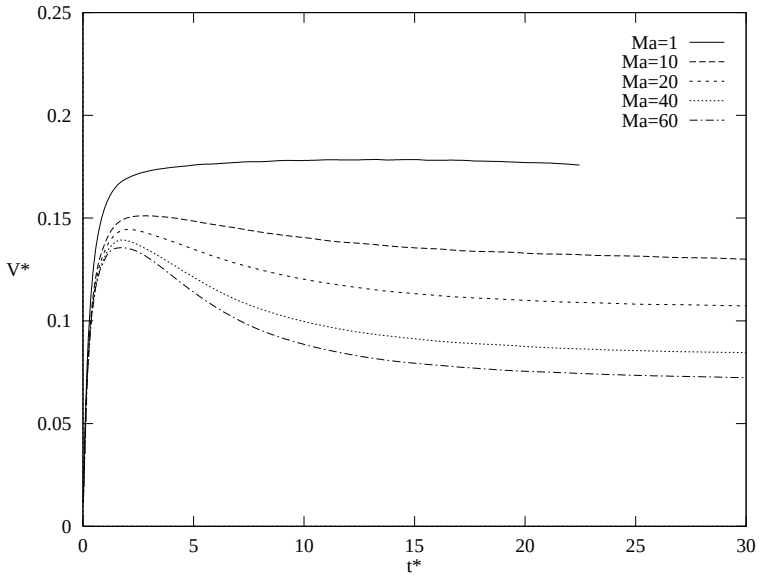

(a) Migration velocity

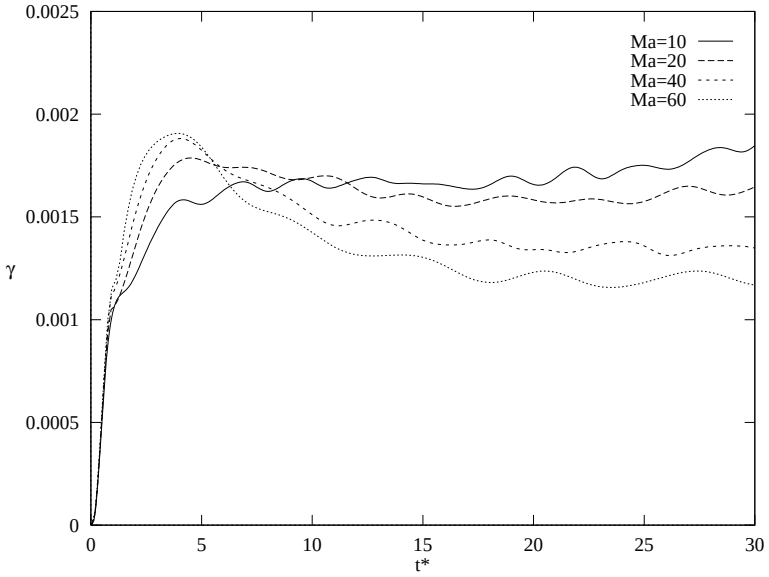

(b) Deformation

Figure 3.4: Effect of Marangoni number on the migration velocity and the deformation of a single bubble.(a) Migration velocity versus time (b) Deformation versus time.

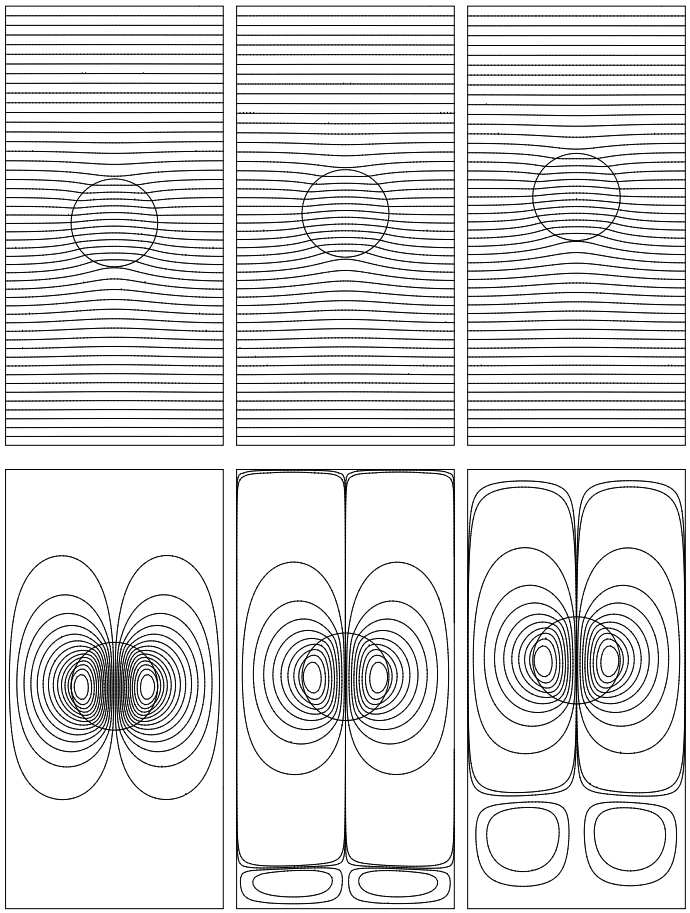

Figure 3.5: Isotherms (top) and streamlines (bottom) of a single bubble migrating at steady state for different Reynolds number. 50 equally spaced isotherms and 20 equally spaced streamlines are shown. Reynolds number for each column from left to right is $1, 5, 10$. Here, $Ma = 1$ and $Ca = 0.06666$ and the resolution is 64×128 grid points.

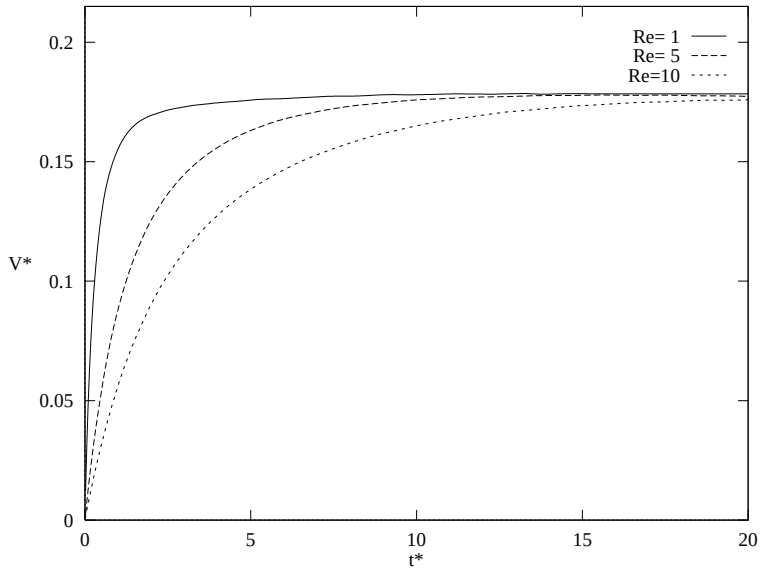

(a) Migration velocity

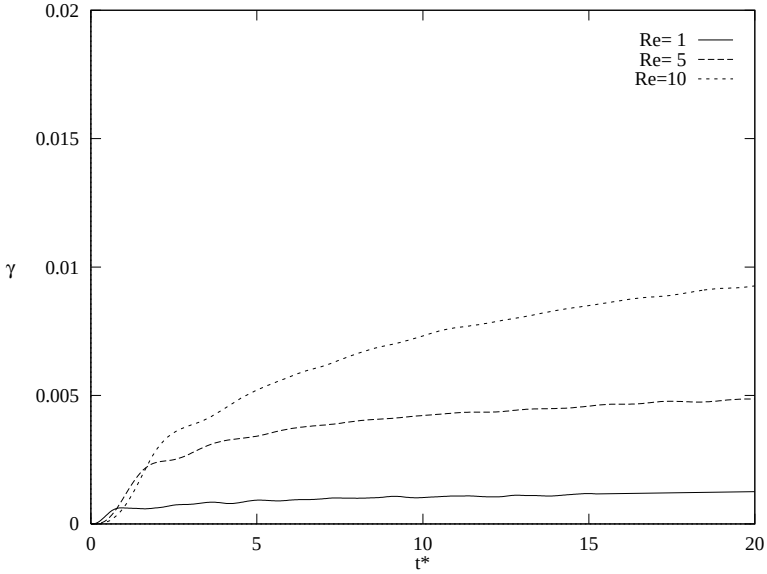

(b) Deformation

Figure 3.6: Effect of Reynolds number on the migration velocity and the deformation of a single bubble. (a) Migration velocity (b) Deformation versus time. Here, $Ma = 1$ and $Ca = 0.06666$.

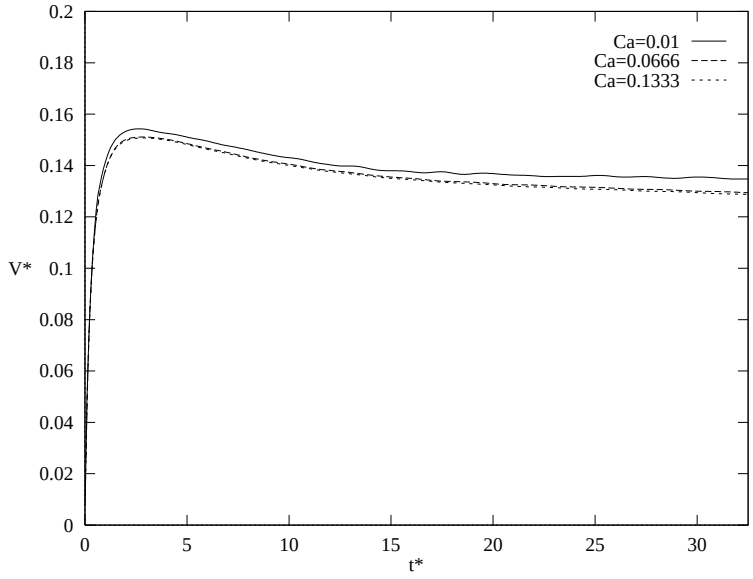

(a) Migration velocity

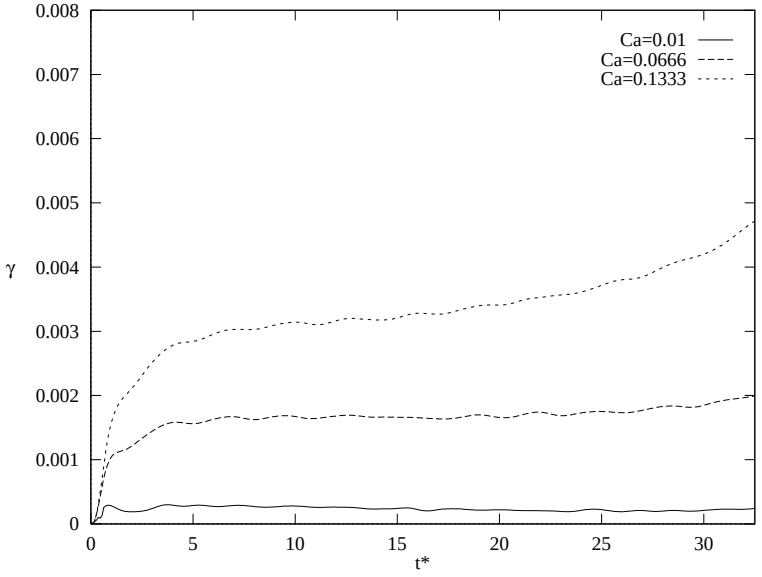

(b) Deformation

Figure 3.7: Effect of Capillary number on the migration velocity and the deformation of a single bubble. (a) Migration velocity (b) Deformation versus time. Here, $Re = Ma = 1$.

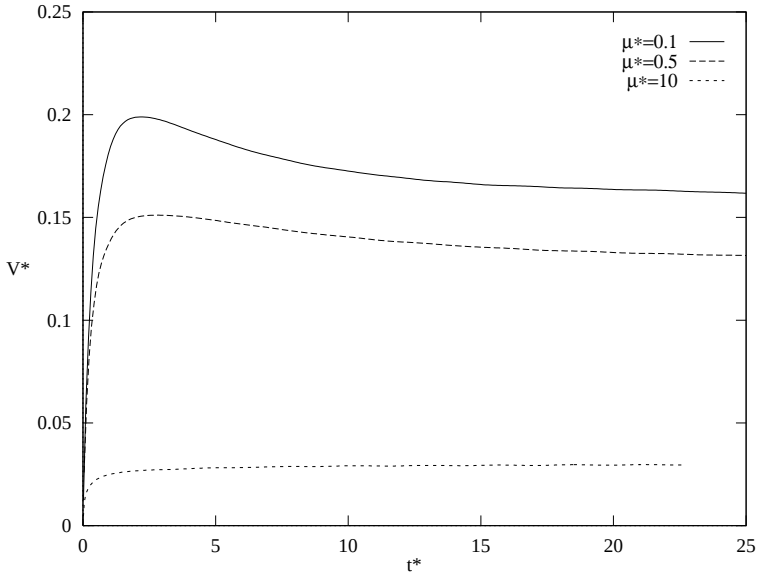

(a) Effect of the viscousity ratio

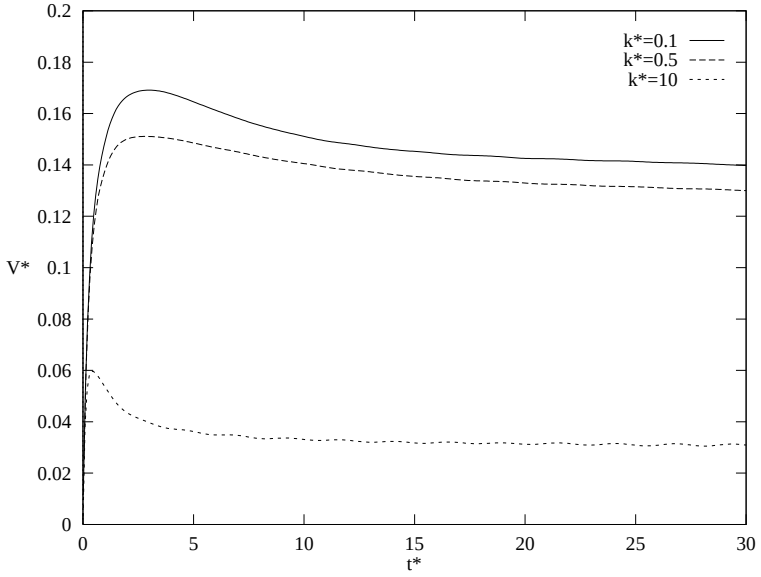

(b) Effect of the conductivity ratio

Figure 3.8: (a) The effect of the viscousity ratio and (b) the effect of the conductivity ratio on the migration velocity of a bubble. Here, $Re = Ma = 1$ and $Ca = 0.06666$.

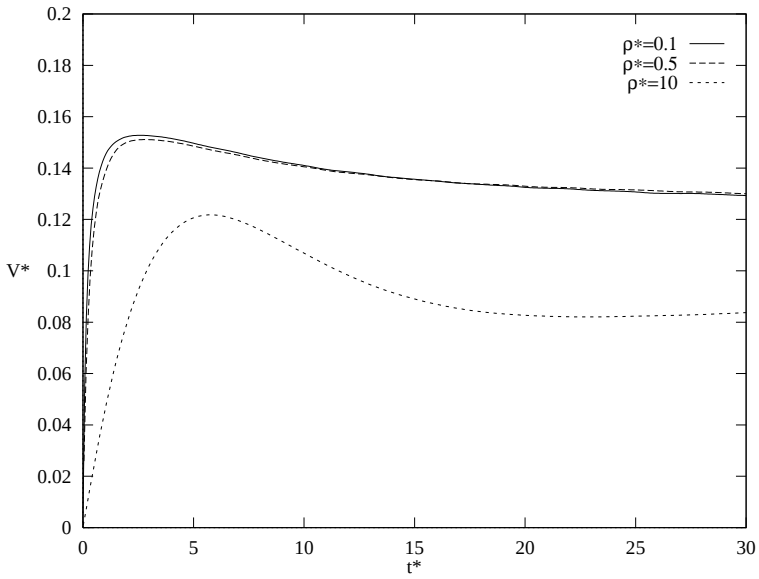

(a) Effect of the density ratio

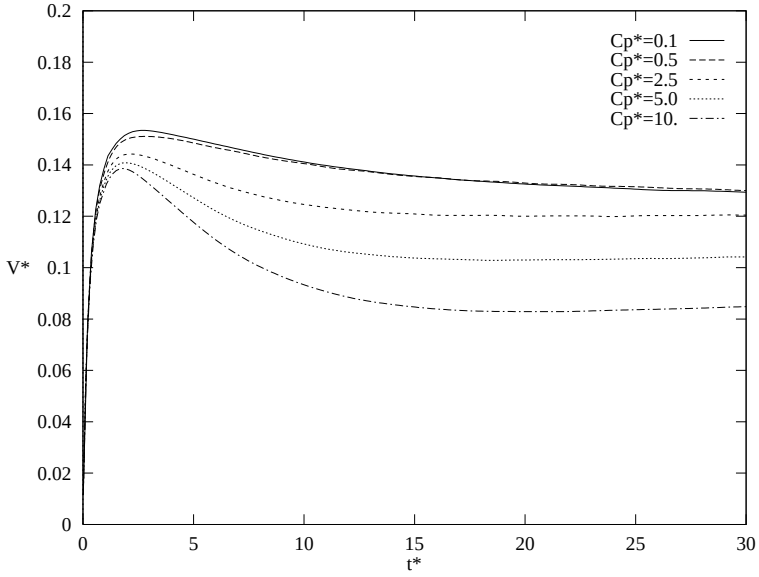

(b) Effect of the heat capacity ratio

Figure 3.9: (a) The effect of the density ratio and (b) the effect of the heat capacity ratio on the migration velocity of a single bubble. Here, $Re = Ma = 1$ and $Ca = 0.06666$.

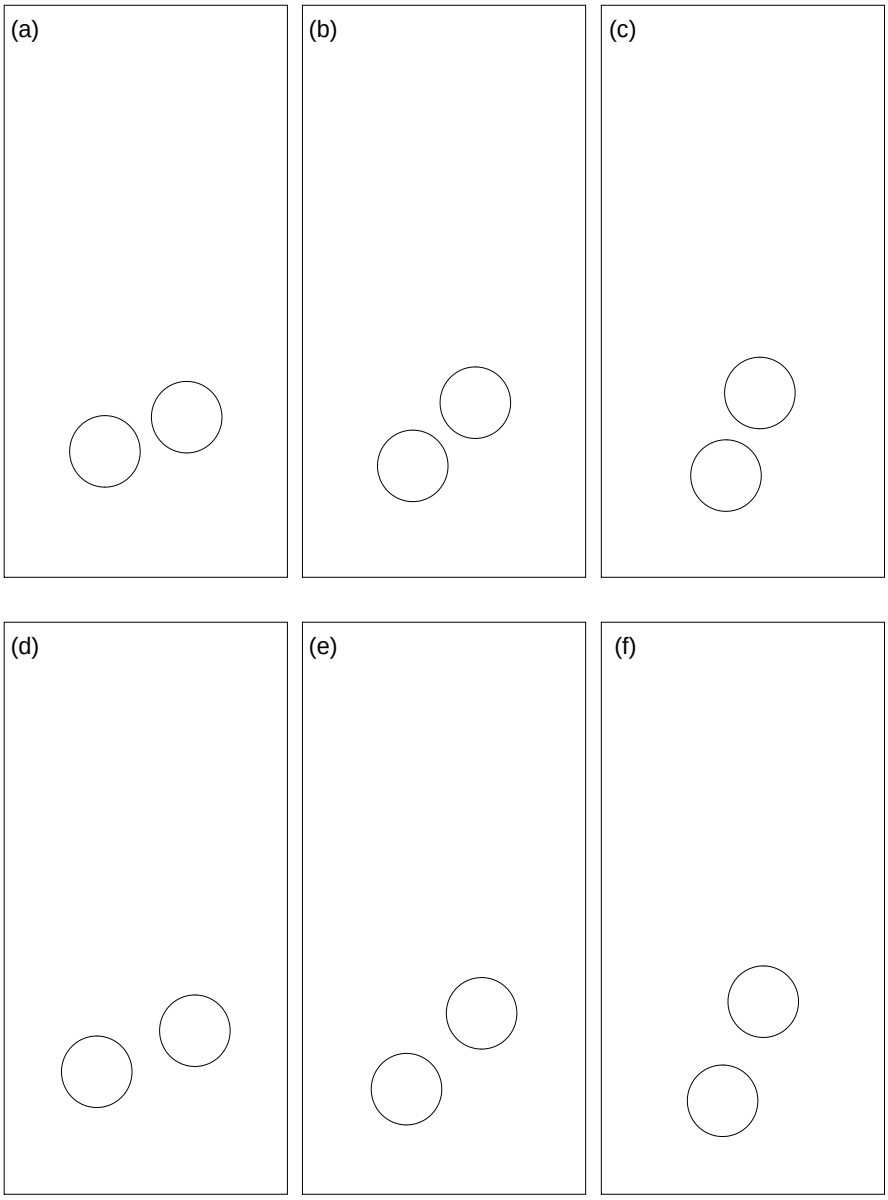

Figure 3.10: 6 different initial position for two-bubble interaction. Computational domain size is $x/a = 8$ and $z/a = 16$.

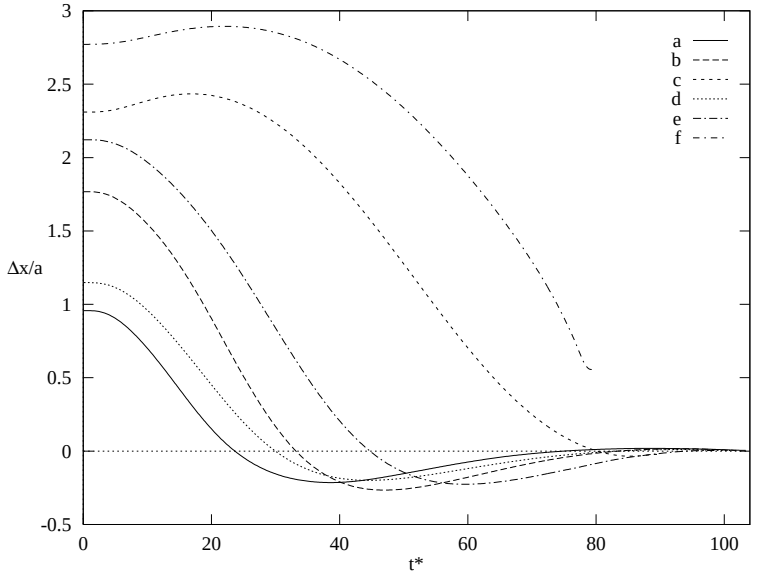

(a) The scaled vertical separation

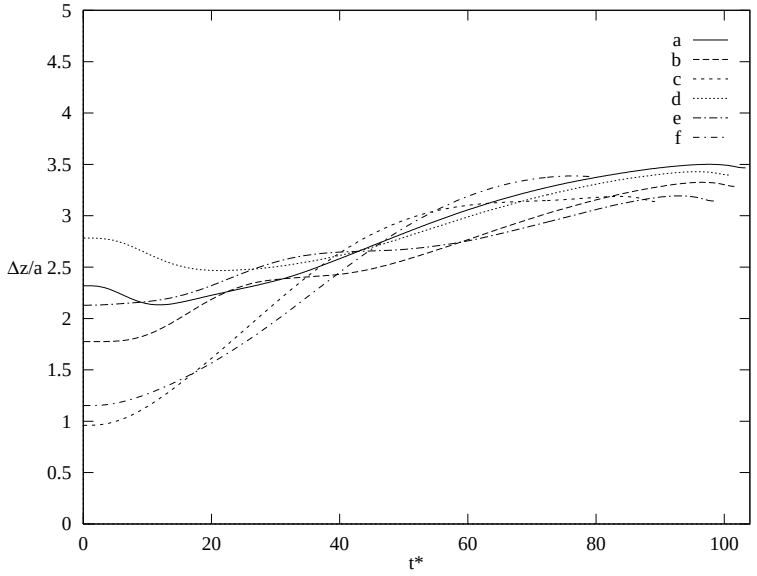

(b) The scaled horizontal separation

Figure 3.11: The scaled (a) vertical (b) horizontal separation between the bubble on the right and the left versus time. The distance is scaled by bubble radius, a and time is scaled by a/U_r.

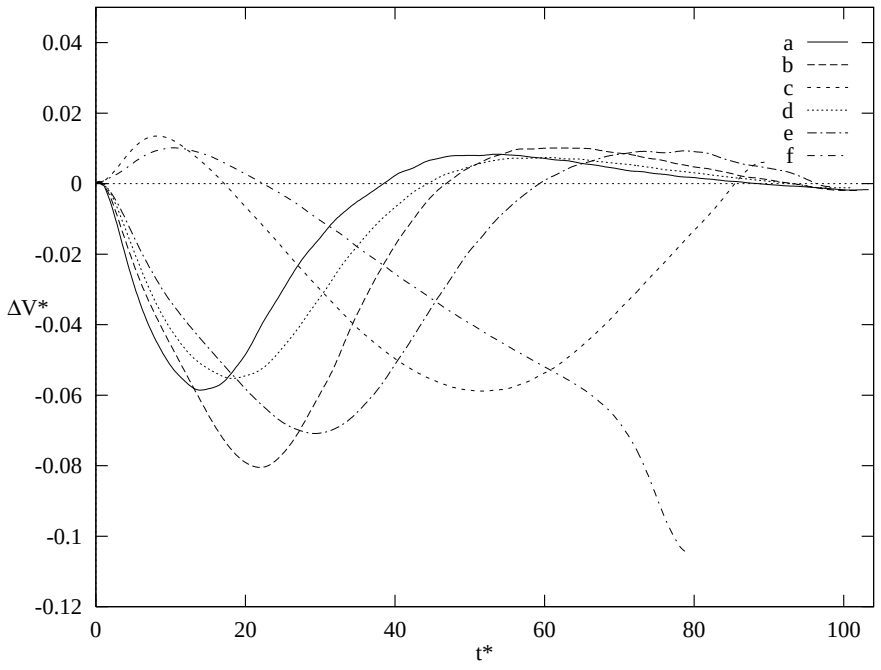

Figure 3.12: The scaled migration velocity difference between the bubble on the right and the left versus time. The velocity difference is scaled by U_r and time is scaled by a/U_r.

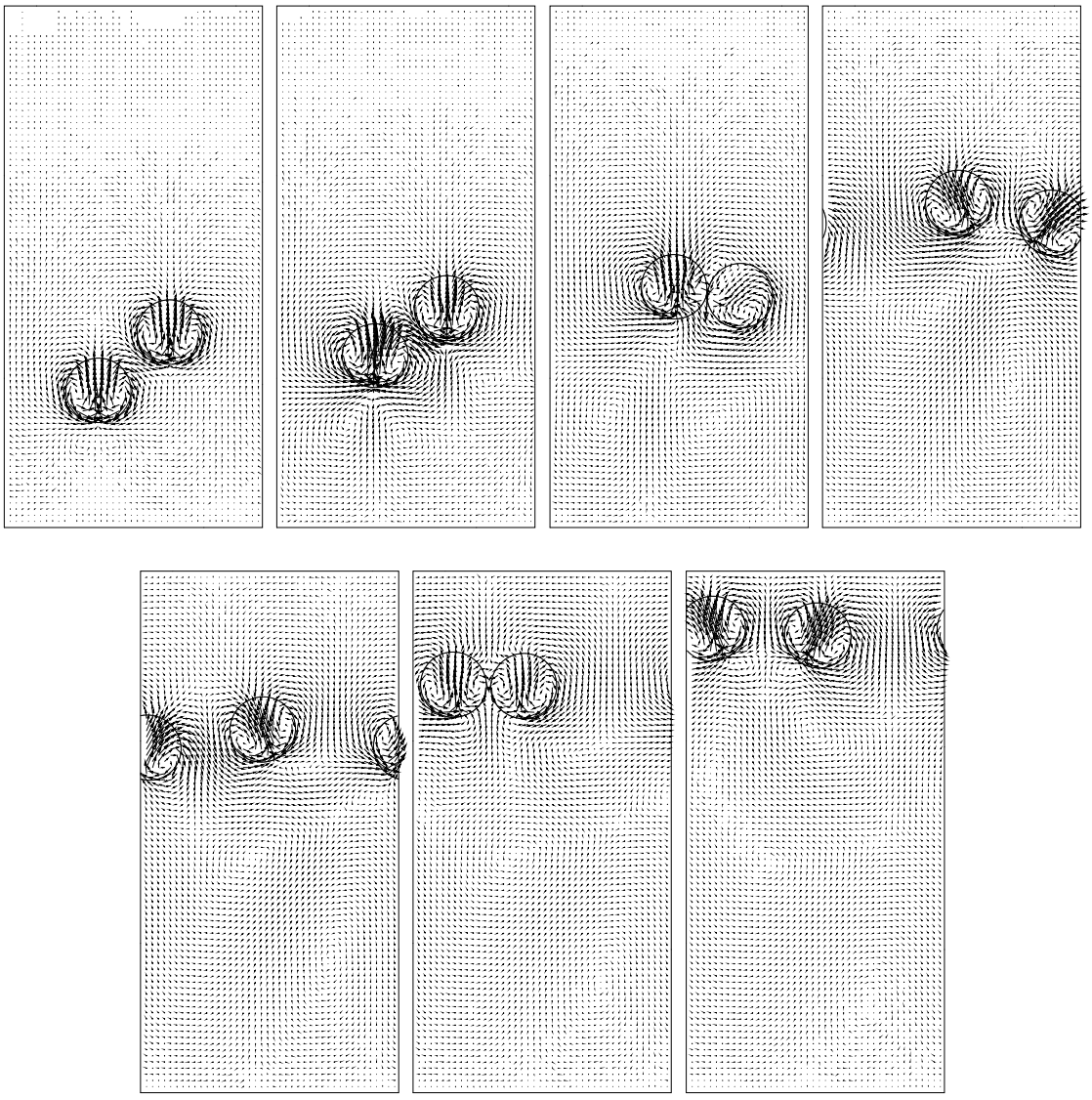

Figure 3.13: Velocity field for selected frames from the computation of two bubble interaction. Only one third of the velocity field is shown. Time progresses from left to right. The nondimensional time, t^*, is equal to $3.8, 11.4, 25.3, 56.9, 69.5, 88.5, 107.5$. The nondimensional time is scaled by a/U_r and velocity is scaled by reference velocity, U_r. Computational domain size is $x/a = 8$ and $z/a = 16$.

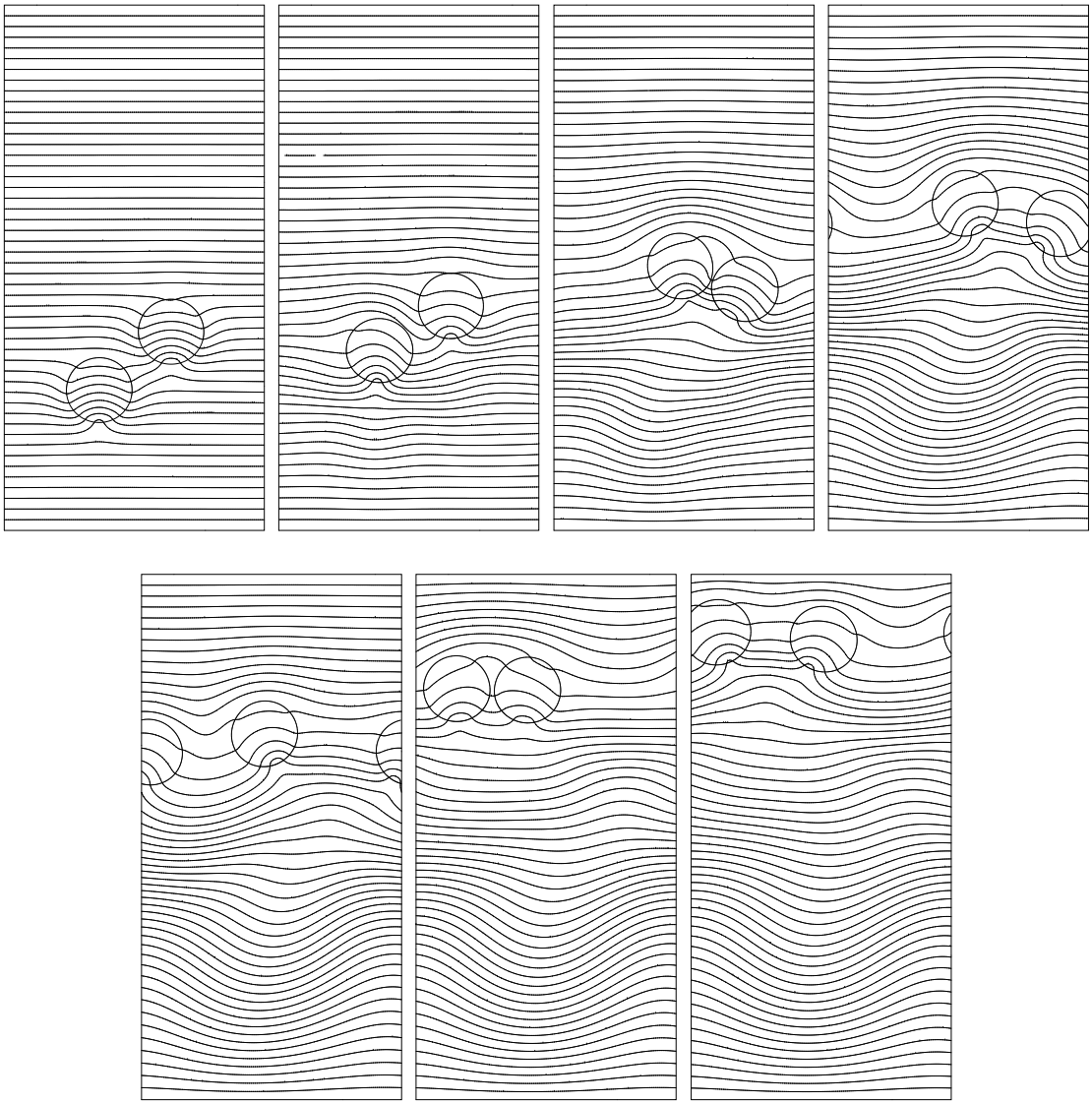

Figure 3.14: Temperature contours for selected frames from the computation of two bubble interaction. 50 equally spaced contours are shown. Time progresses from left to right. The nondimensional time, t^*, is equal to $3.8, 11.4, 25.3, 56.9, 69.5, 88.5, 107.5$. The nondimensional time is scaled by a/U_r and temperature is scaled, after subtracting a reference temperature, by $a\nabla T_\infty$. Computational domain size is $x/a = 8$ and $z/a = 16$. Here, $Re = Ma = 40$ and $Ca = 0.04166$.

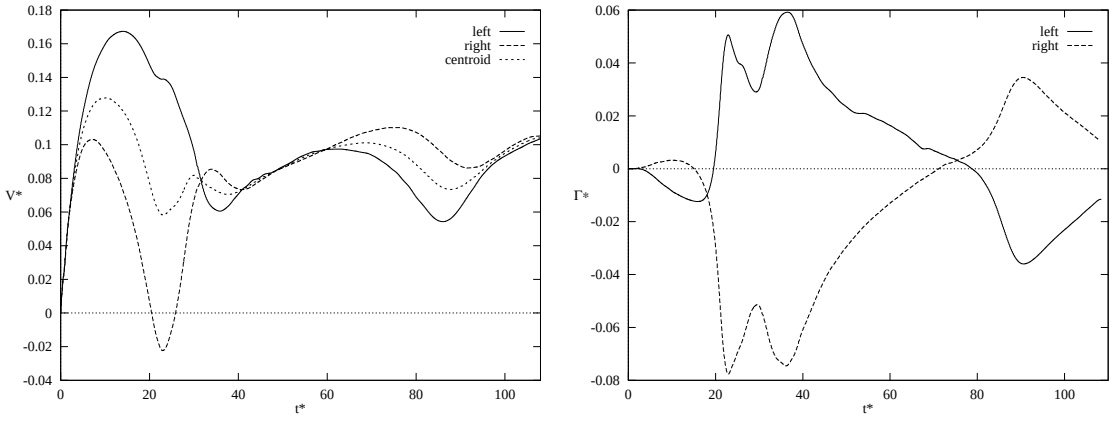

(a) Migration velocity

(b) Internal circulation

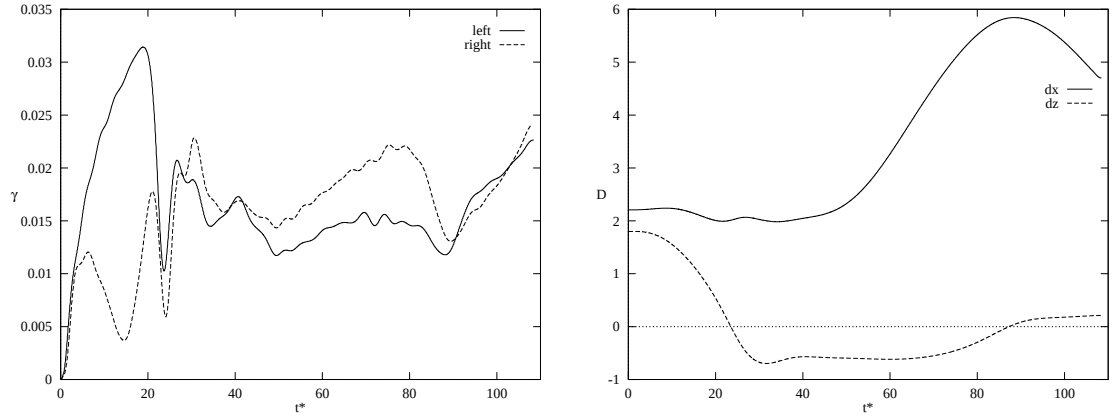

(c) Deformation

(d) Seperation distance

Figure 3.15: Quantitative description of the two bubble interaction in Figure 3.13 and 3.14. (a) Migration velocity versus time. (b) Internal circulation versus time. (c) Deformation versus time. (d) Seperation distance versus time. Velocity is scaled by U_r, separation distance by a, time by a/U_r, and the internal circulation by $2\pi a U_r$.

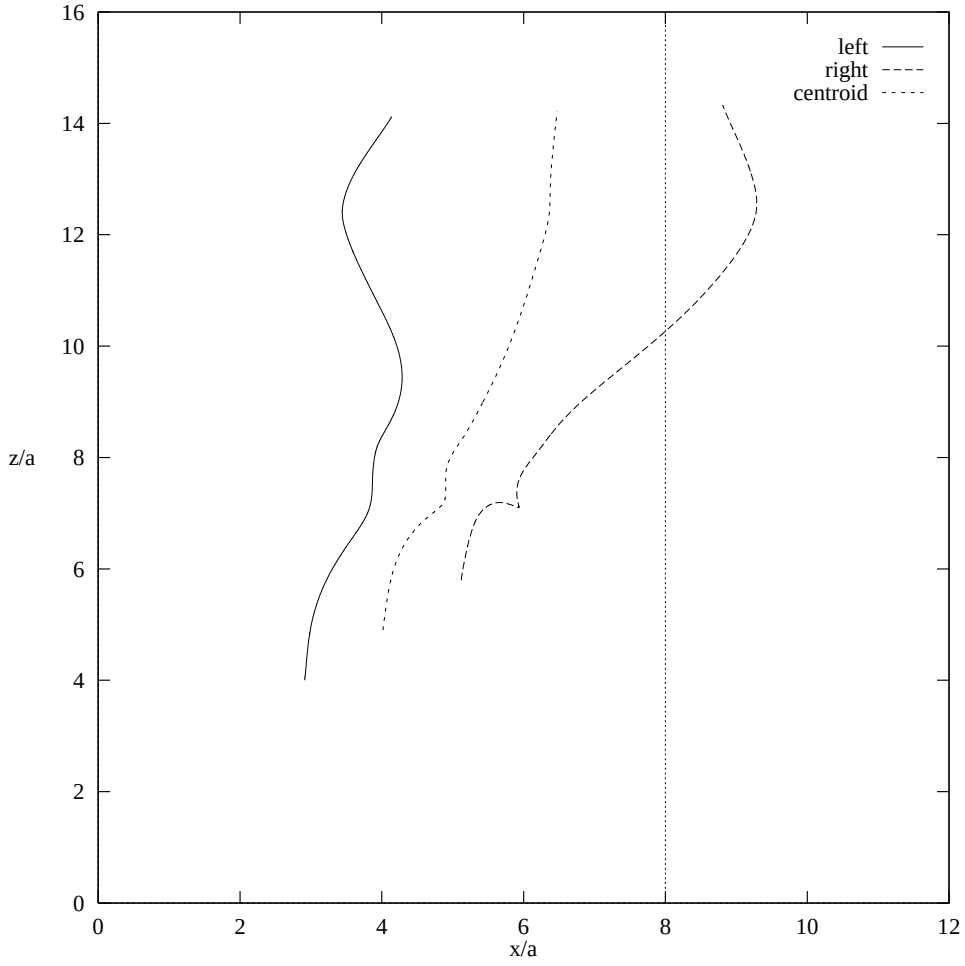

Figure 3.16: Trajectories of the center of mass of the bubbles in Figure 3.13 and 3.14. Both axis are scaled by the bubble radius a.

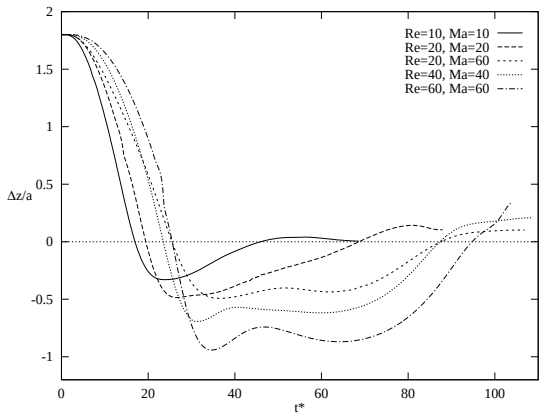

(a) The vertical separation distance

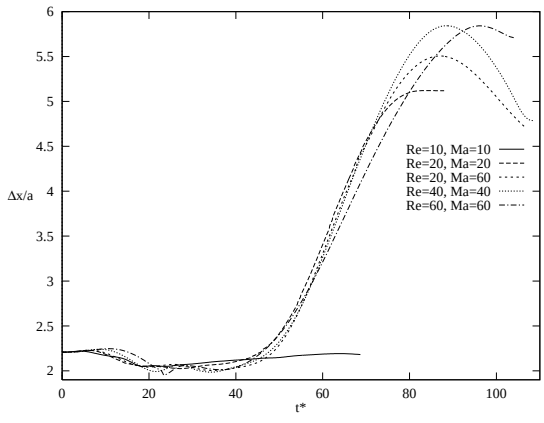

(b) The horizontal separation distance

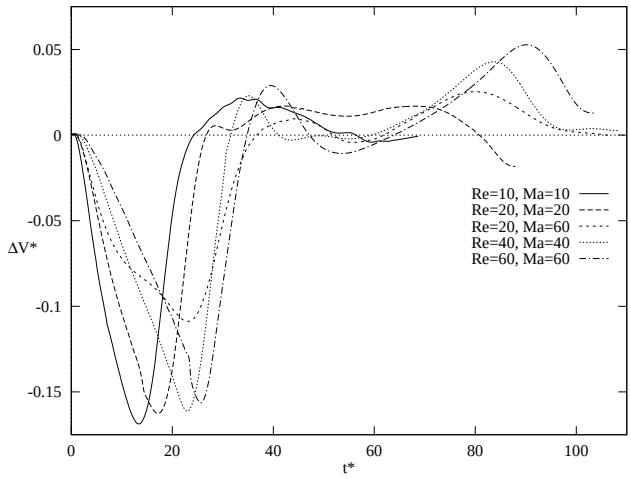

(c) The migration velocity difference

Figure 3.17: Quantitative information about two-bubble interaction for different Reynolds and Marangoni numbers. (a) The vertical separation distance versus time. (b) The horizontal separation distance versus time. (c) The migration velocity difference versus time. Time is scaled by a/U_r, separation difference, Δ, by, a, and the velocity difference by U_r. The differences are between the bubble on the right and the left.

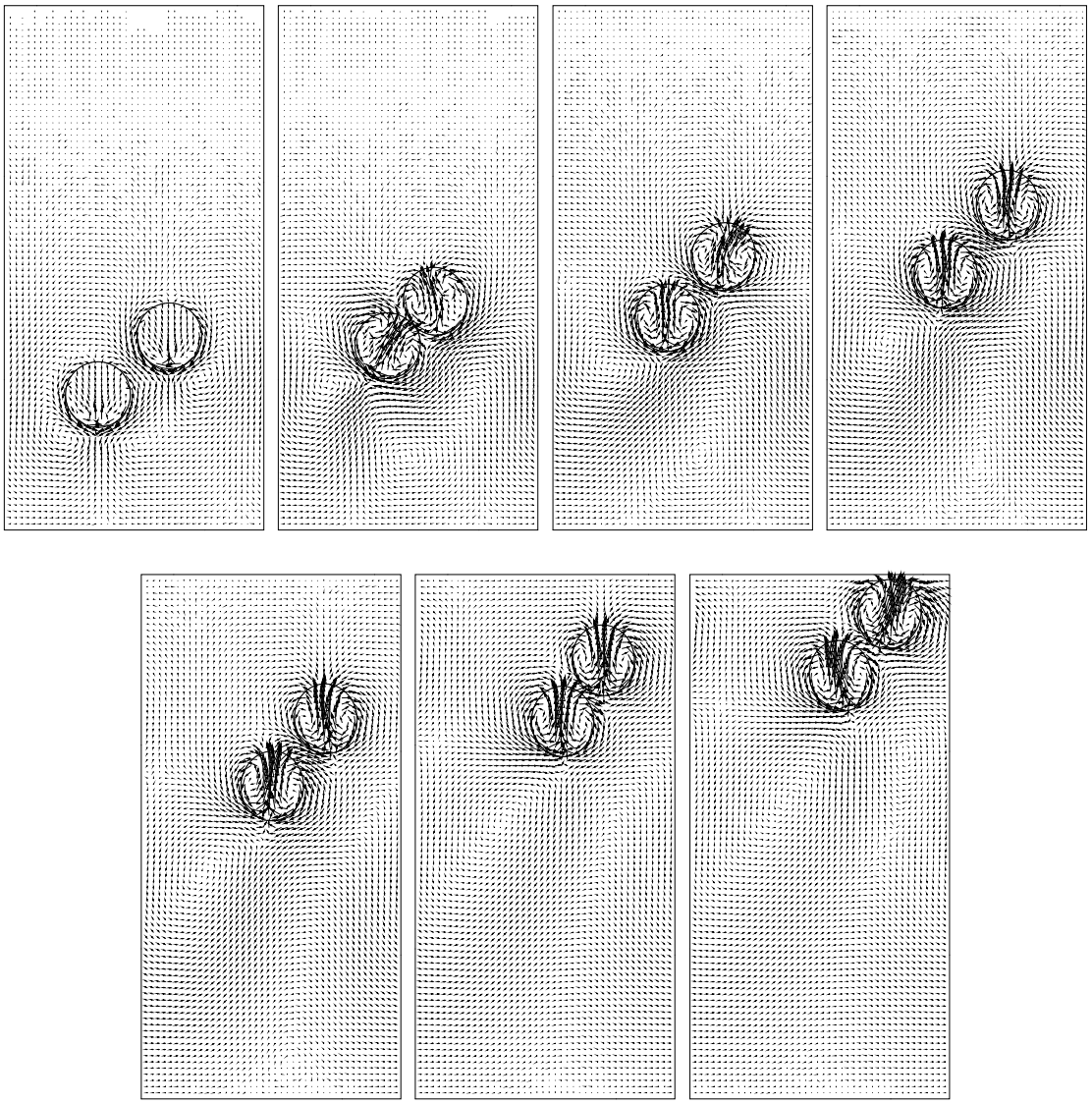

Figure 3.18: Velocity field for selected frames from the computation of two drop interaction. The velocity field is shown at every third grid point. Time progresses from left to right. The nondimensional time, t^*, is equal to $12.65, 50.60, 75.89, 101.19, 126.49, 151.79, 170.0$. The nondimensional time is scaled by a/U_r and velocity is scaled by reference velocity, U_r. Computational domain size is $x/a = 8$ and $z/a = 16$. Here, $Re = Ma = 40$ and $Ca = 0.04166$.

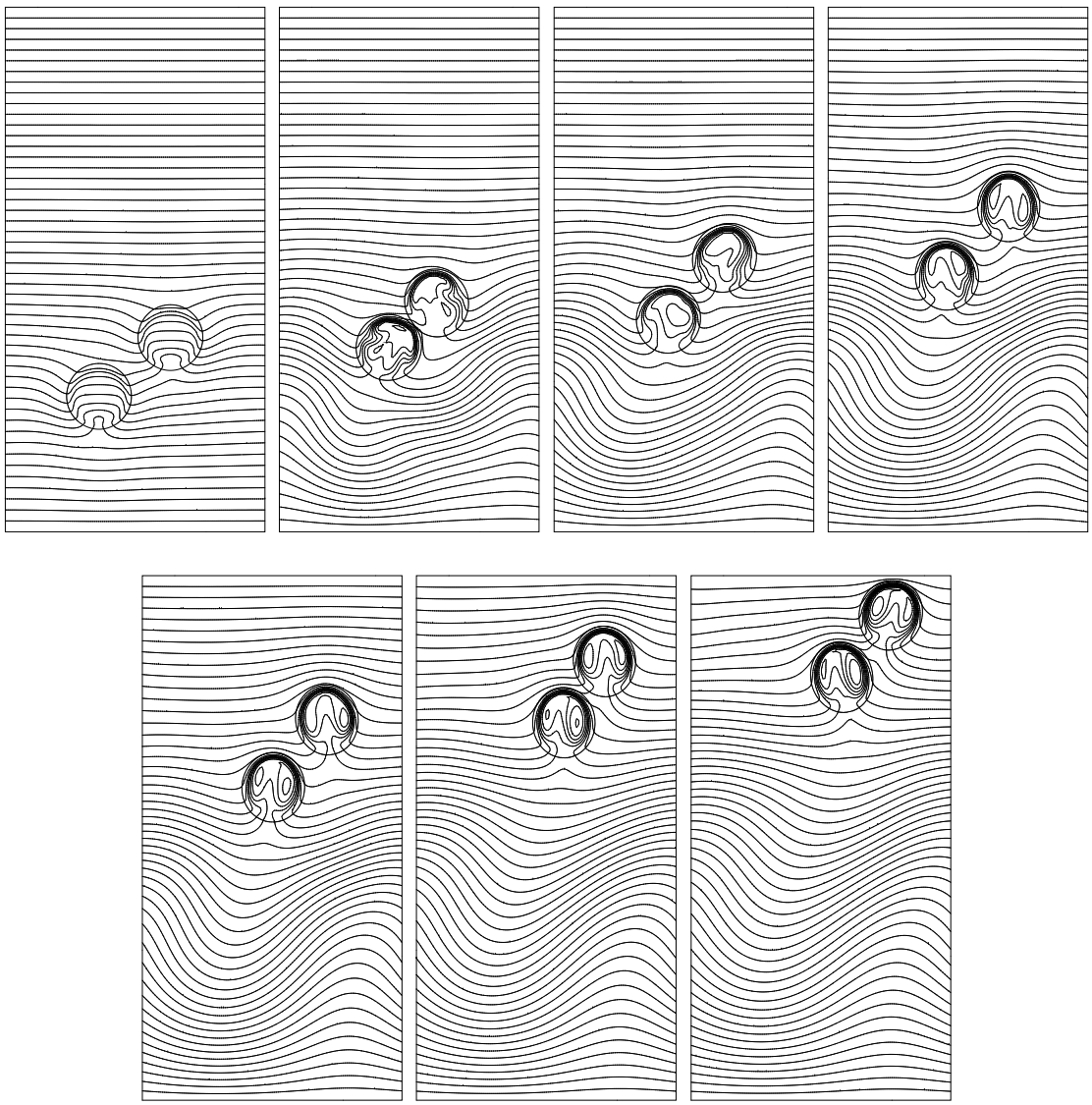

Figure 3.19: Temperature contours for selected frames from the computation of two drop interaction in Figure 3.18. 50 equally spaced contours are shown. Time progresses from left to right. The nondimensional time, t^*, is equal to $12.65, 50.60, 75.89, 101.19, 126.49, 151.79, 170.0$. The nondimensional time is scaled by a/U_r and temperature is scaled, after subtracting a reference temperature, by $a\nabla T_\infty$. Computational domain size is $x/a = 8$ and $z/a = 16$.

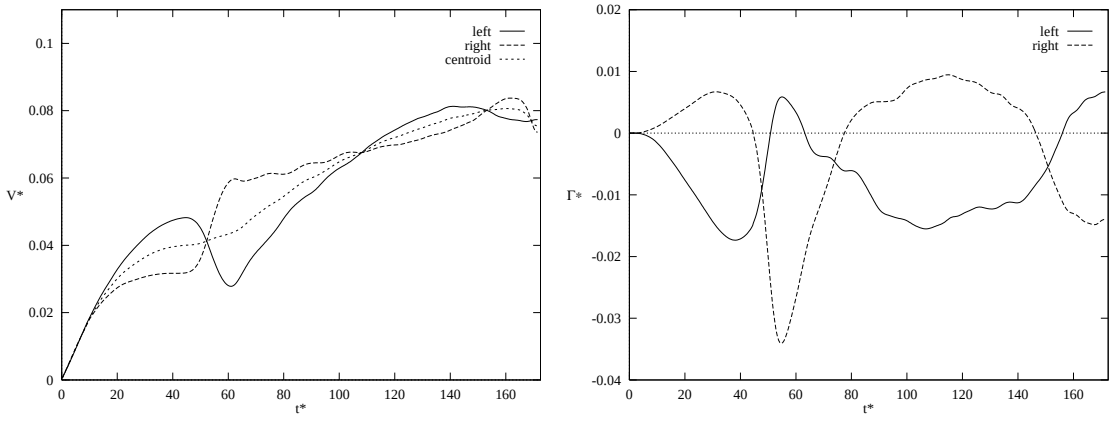

(a) Migration velocity

(b) Internal circulation

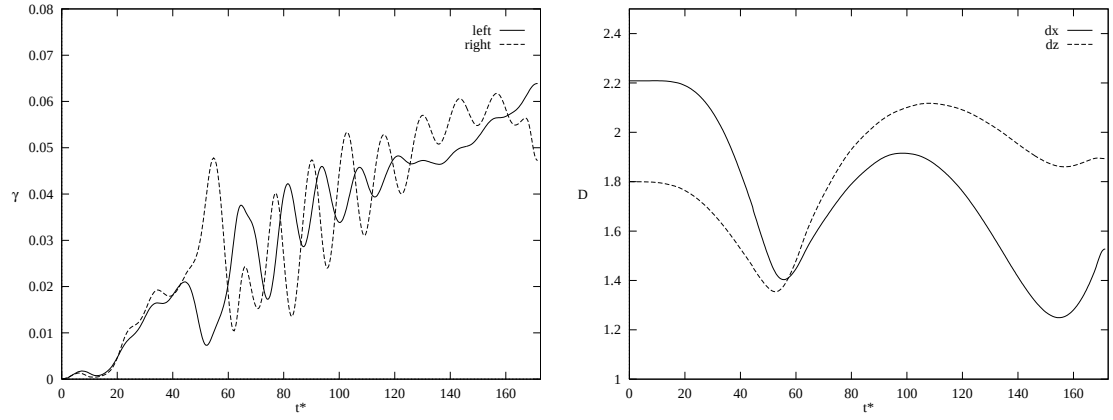

(c) Deformation

(d) Separation distance

Figure 3.20: Quantitative description of the two drop interaction in Figures 3.18 and 3.19. (a) Migration velocity versus time. (b) Internal circulation versus time. (c) Deformation versus time. (d) Separation distance versus time. Velocity is scaled by U_r, separation distance by a, time by a/U_r, and the internal circulation by $2\pi a U_r$.

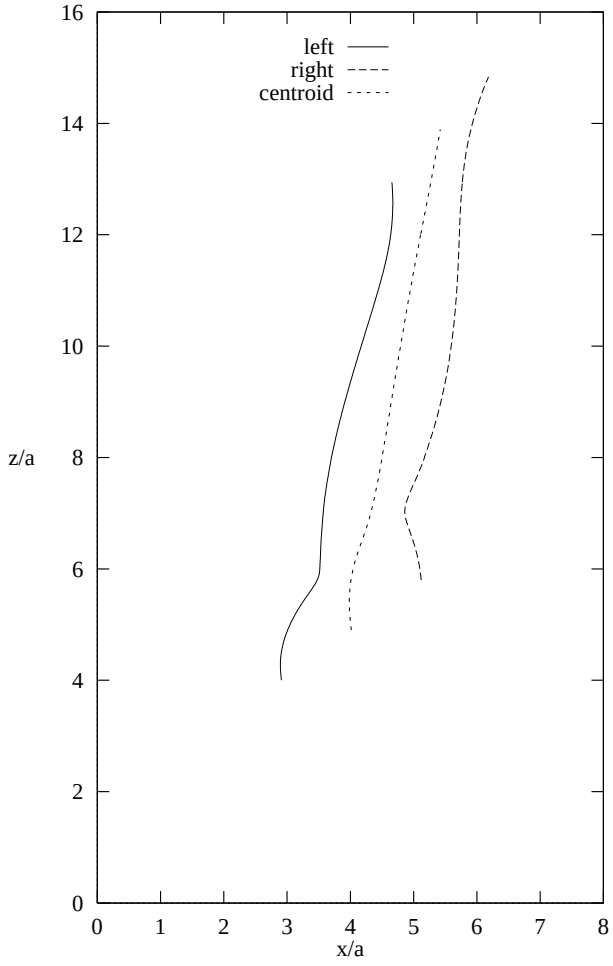

Figure 3.21: Trajectories of the center of mass of drops in Figures 3.18 and 3.19. Both axis are scaled by the drop radius a.

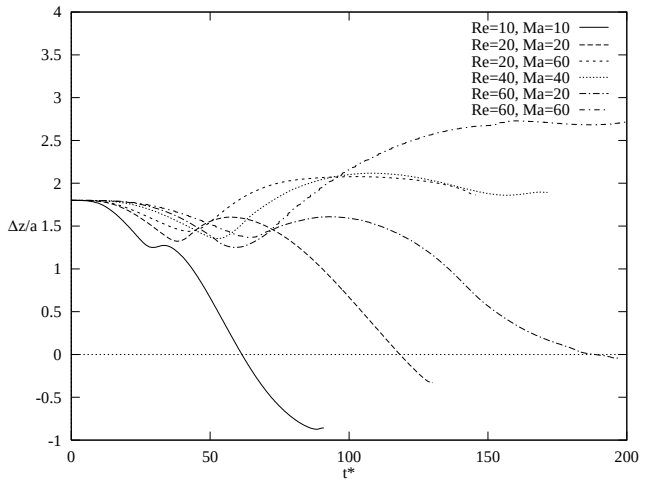

(a) The vertical separation distance

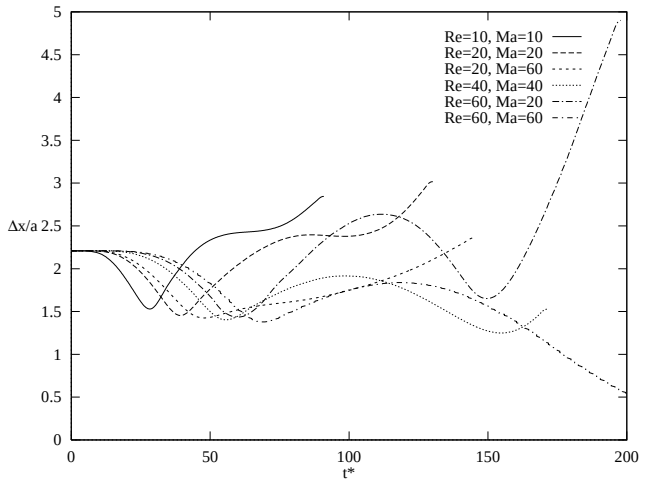

(b) The horizontal separation distance

Figure 3.22: Quantitative information for two-drop interactions for different Reynolds and Marangoni numbers. (a) The vertical separation distance versus time. (b) The horizontal separation distance versus time. Time is scaled by a/U_r, separation difference, Δ, by, a. The differences are between the drop on the right and drop on the left.

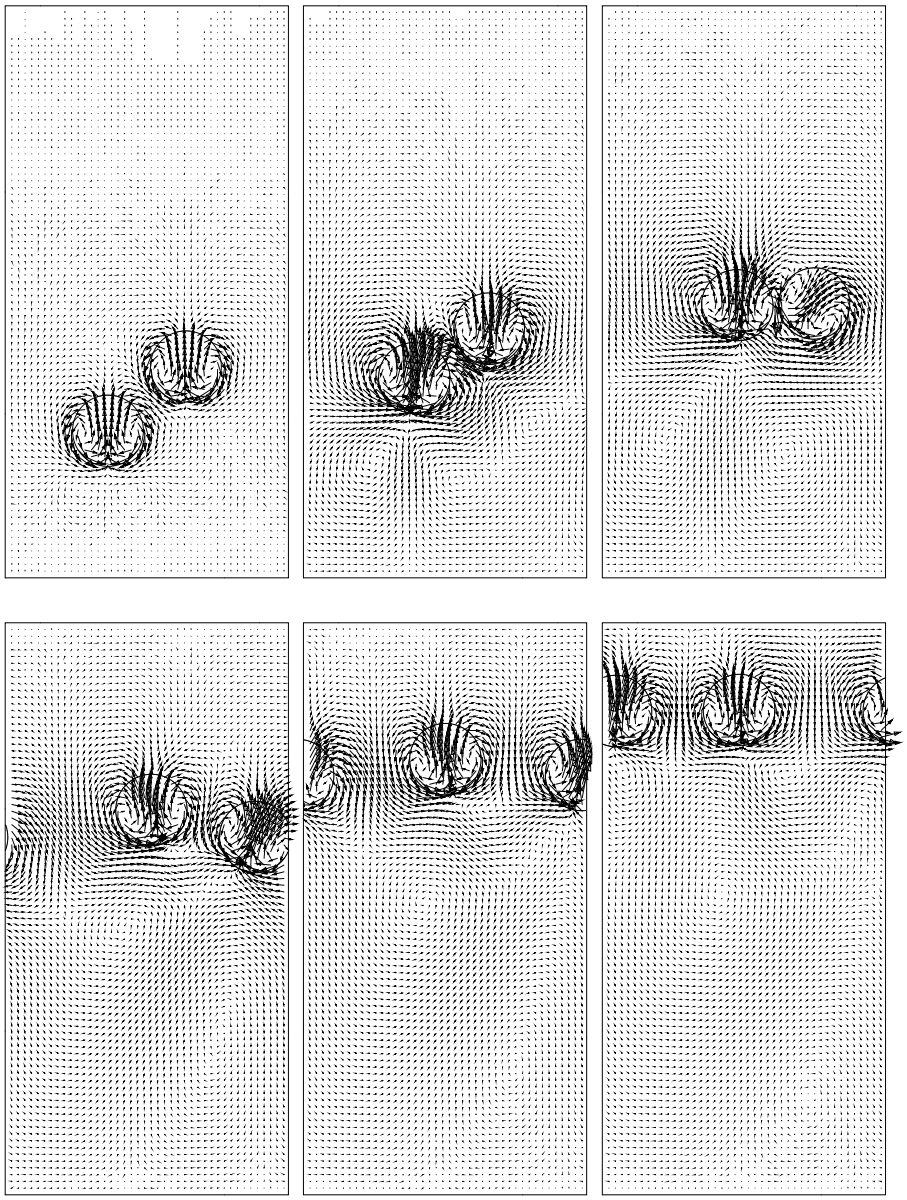

Figure 3.23: Velocity field for selected frames from the computation of two bubble interaction. The velocity field is shown at every third grid point. Time progresses from left to right. The nondimensional time, t^*, is equal to $4, 20, 40, 80, 100, 120$. The nondimensional time is scaled by a/U_r and velocity is scaled by reference velocity, U_r. Computational domain size is $x/a = 8$ and $z/a = 16$. Here, $Re = Ma = 40$ and $Ca = 0.04166$.

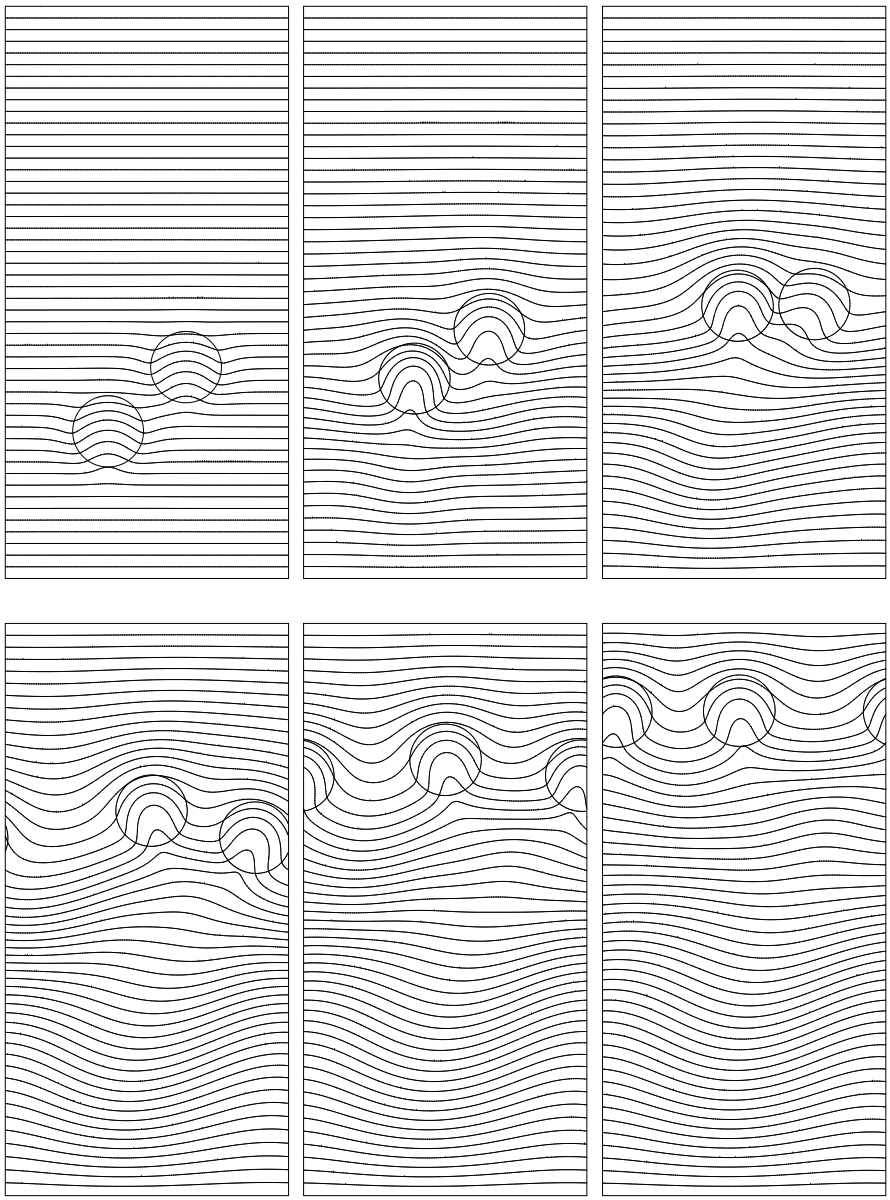

Figure 3.24: Temperature contours for selected frames from the computation of two bubble interaction in Figure 3.23. 50 equally spaced contours are shown. Time progresses from left to right. The nondimensional time, t^*, is equal to $4, 20, 40, 80, 100, 120$. The nondimensional time is scaled by a/U_r and temperature is scaled, after subtracting a reference temperature, by $a\nabla T_\infty$. Computational domain size is $x/a = 8$ and $z/a = 16$.

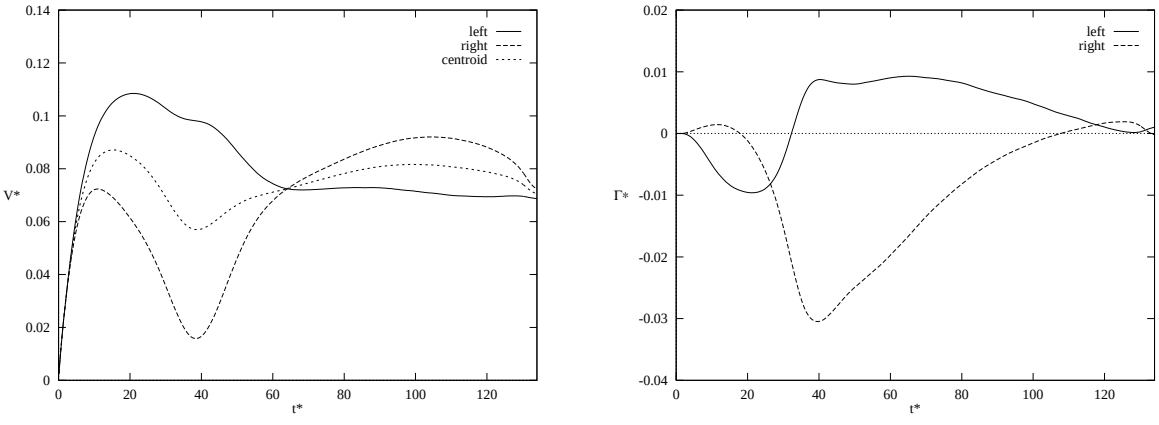

(a) Migration velocity

(b) Internal circulation

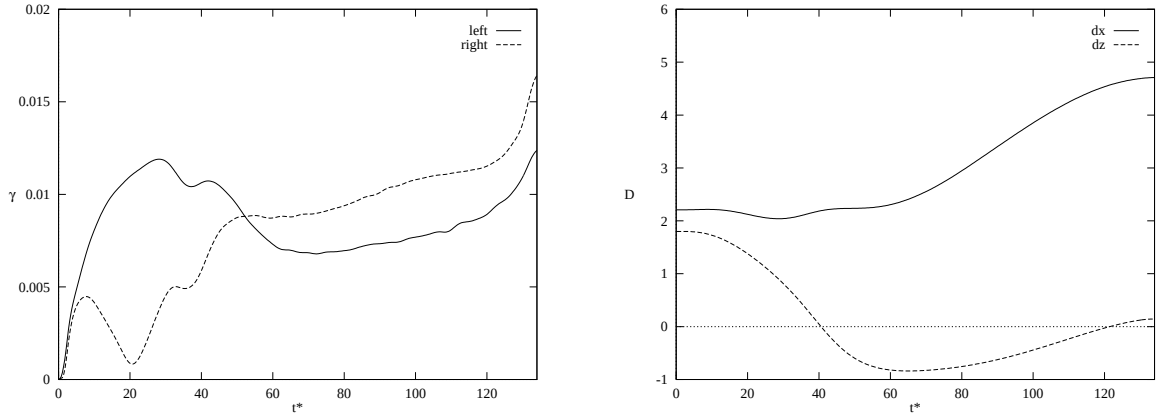

(c) Deformation

(d) Separation distance

Figure 3.25: Quantitative description of the two bubble interaction in Figures 3.23 and 3.24. (a) Migration velocity versus time. (b) Internal circulation versus time. (c) Deformation versus time. (d) Separation distance versus time. Velocity is scaled by U_r, separation distance by a, time by a/U_r, and the internal circulation by $2\pi a U_r$.

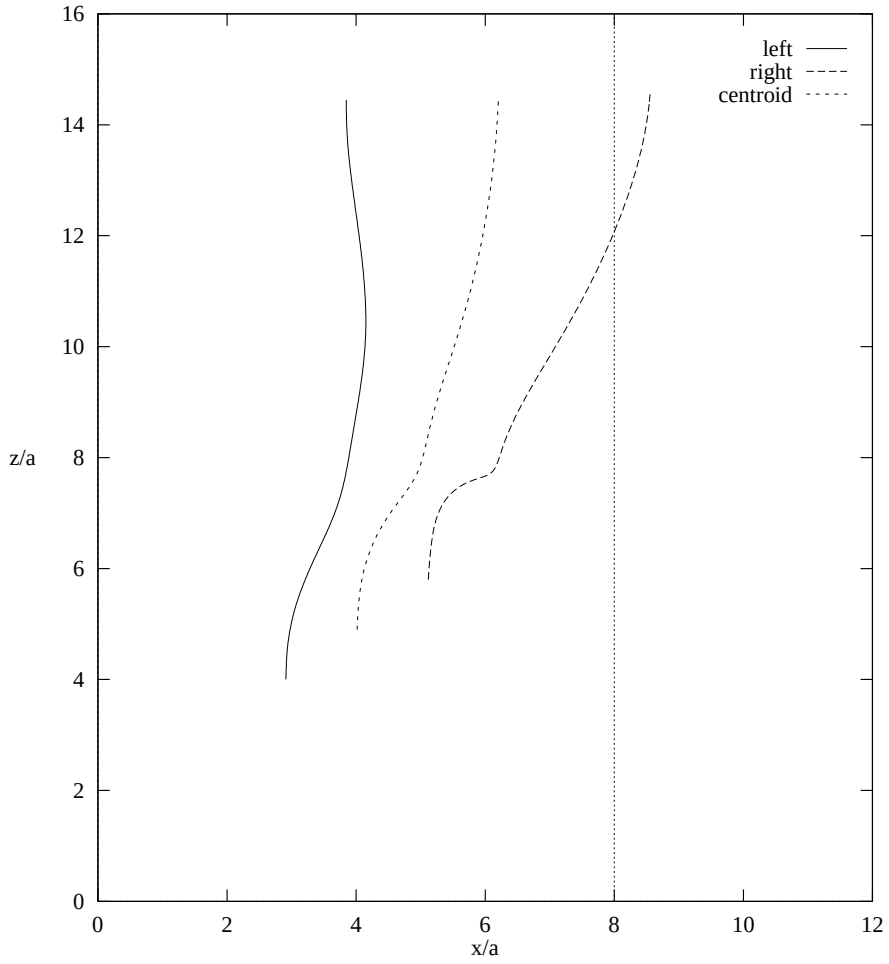

Figure 3.26: Trajectories of the center of mass of the bubbles in Figures 3.23 and 3.24. Both axis are scaled by the bubble radius a.

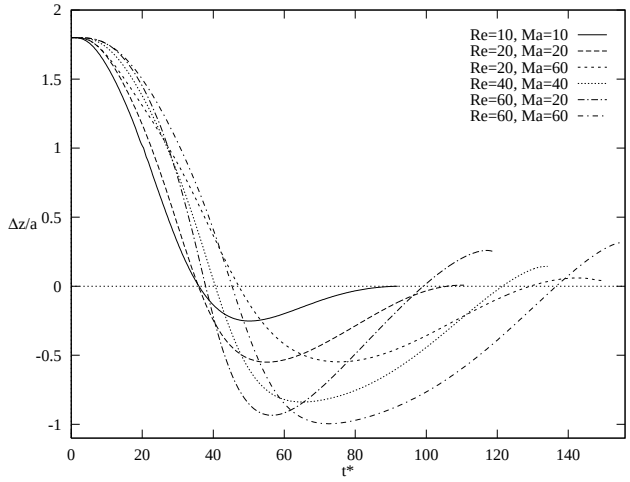

(a) The vertical separation distance

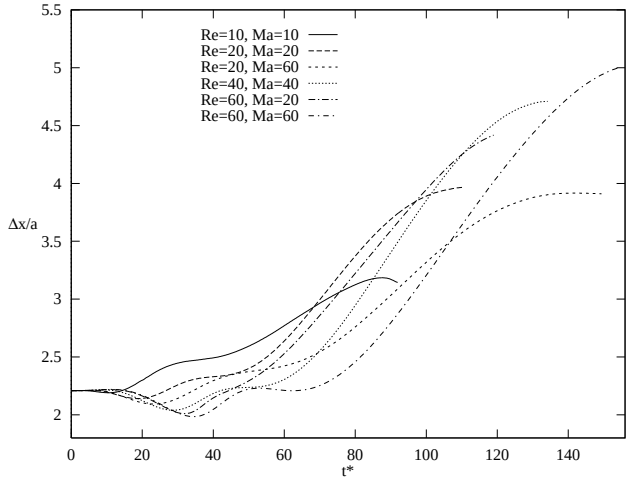

(b) The horizontal separation distance

Figure 3.27: Quantitative information for two-bubble interactions for different Reynolds and Marangoni numbers. (a) The vertical separation distance versus time. (b) The horizontal separation distance versus time. Time is scaled by a/U_r, separation difference, D, by, a. The differences are between the bubble on the right and the left.

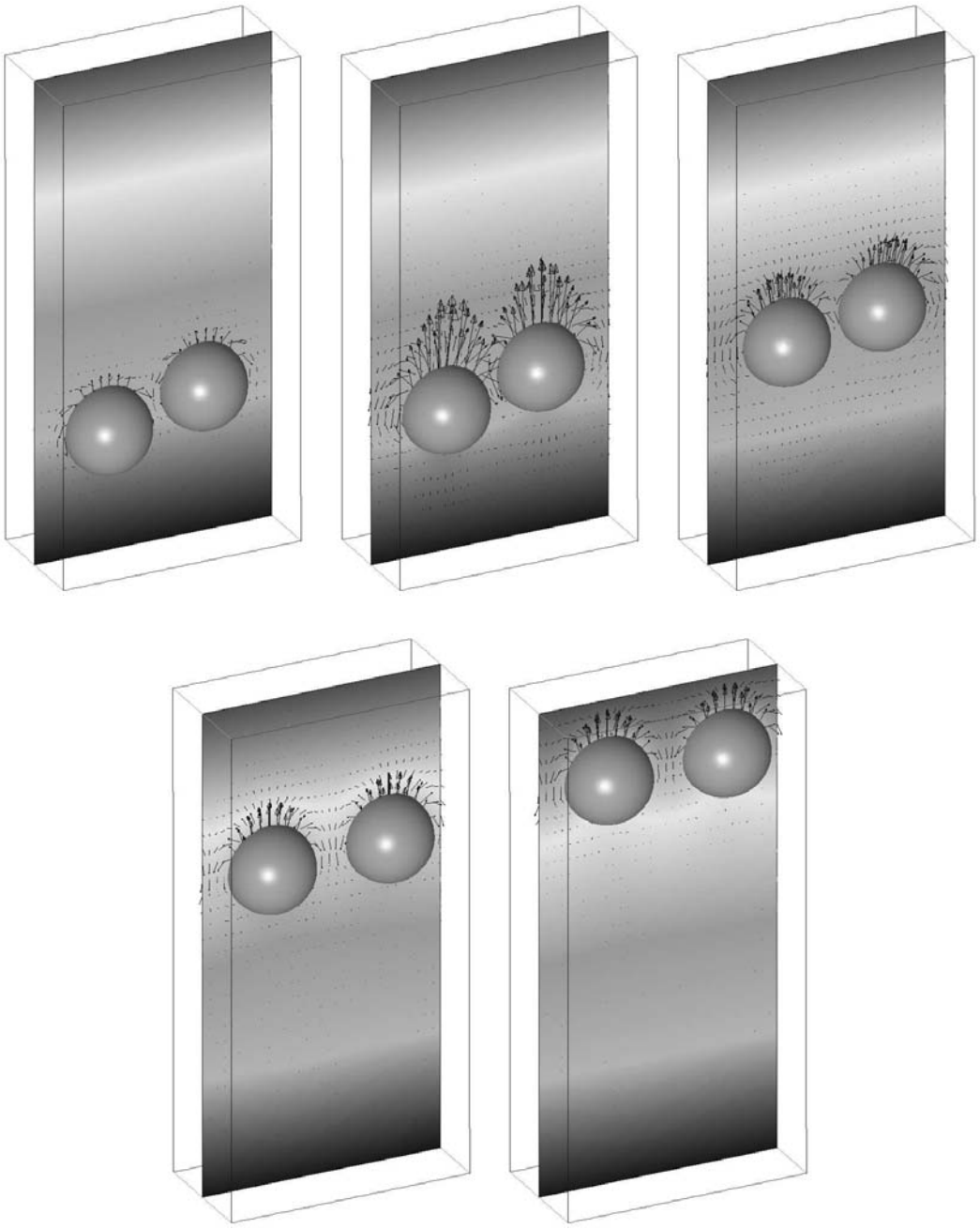

Figure 3.28: Velocity and temperature field for selected frames from the fully three-dimensional simulation of two-bubble interaction. The velocity field is shown at every other grid point in the middle plane of the computational box in y direction. Time progresses from left to right, top to bottom. The nondimensional time, t^*, is equal to $0.57, 5.71, 22.85,\ 57.14, 85.71$. The nondimensional time is scaled by a/U_r and velocity is scaled by reference velocity, U_r. Computational domain size is $x/a = 5.71$, $y/a = 2.86$ and $z/a = 11.43$. Here, $Re = 20$, $Ma = 60$ and $Ca = 0.04166$.

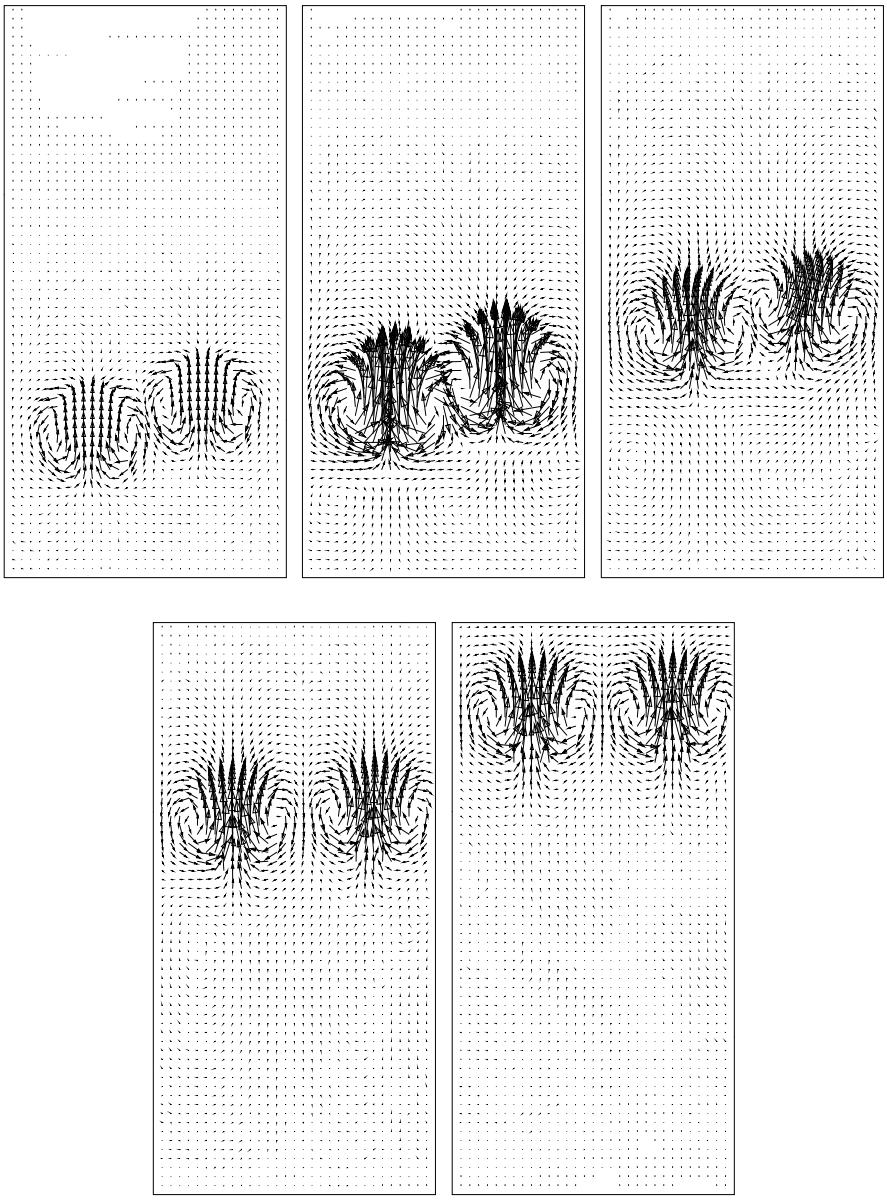

Figure 3.29: Velocity field for selected frames from the fully three dimensional computation of two bubble interaction in Figure 3.28. The velocity field is shown at every other grid point in the middle plane of the computational box in y direction. Time progresses from left to right. The nondimensional time, t^*, is equal to $0.57, 5.71, 22.85, 57.14, 85.71$. The nondimensional time is scaled by a/U_r and velocity by U_r. Computational domain size is $x/a = 5.71$, $y/a = 2.86$ and $z/a = 11.43$.

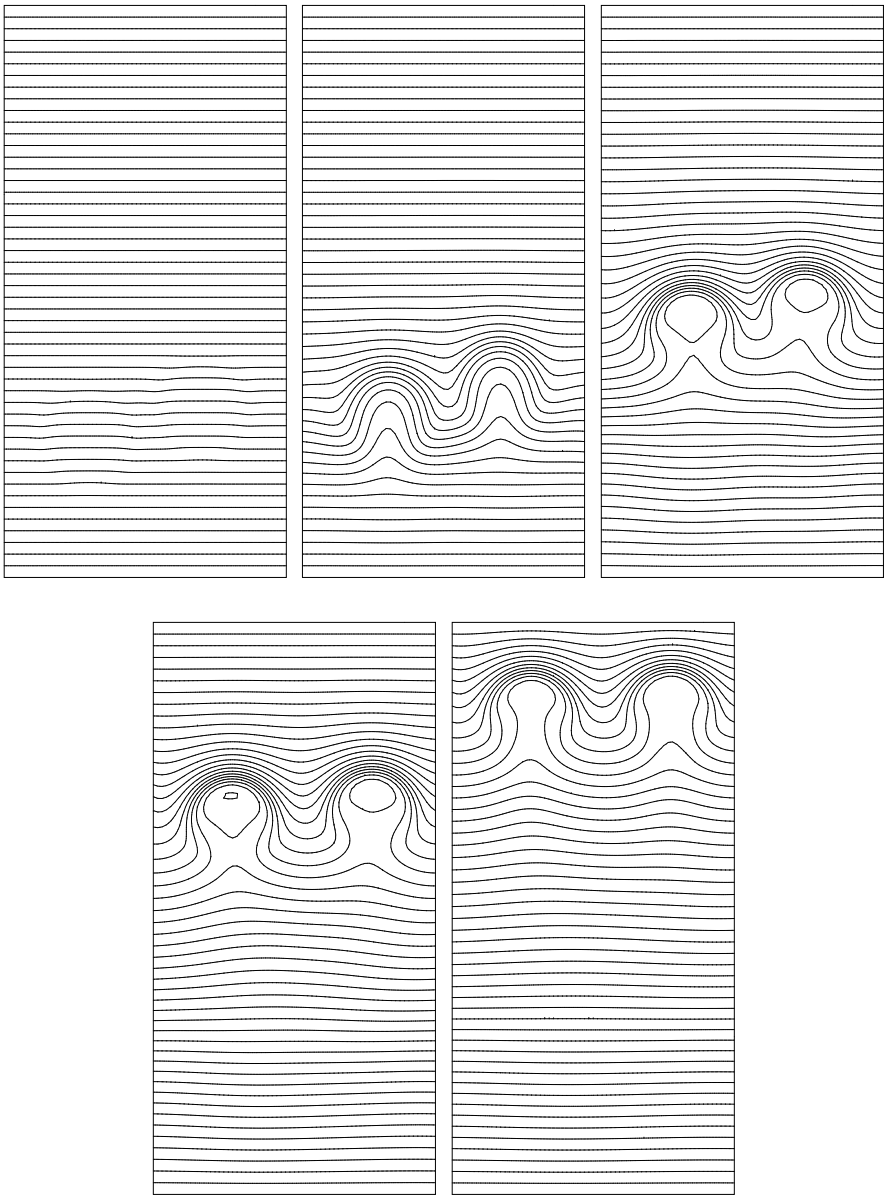

Figure 3.30: Temperature contours for selected frames from the fully three dimensional computation of two bubble interaction in Figure 3.28. 50 equally spaced contours are shown in the middle plane of the computational box in y direction. Time progresses from left to right. The nondimensional time, t^*, is equal to $0.57, 5.71, 22.85, 57.14, 85.71$. The nondimensional time is scaled by a/U_r and temperature is scaled, after subtracting a reference temperature, by $a\nabla T_\infty$. Computational domain size is $x/a = 5.71$, $y/a = 2.86$ and $z/a = 11.43$.

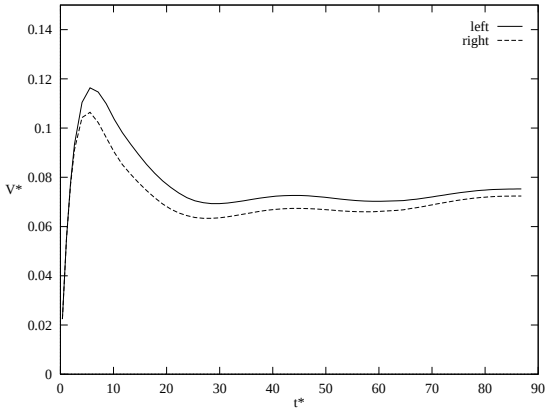

(a) Migration velocity

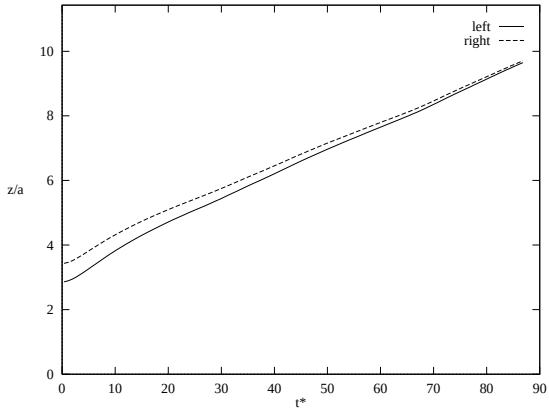

(b) Vertical position

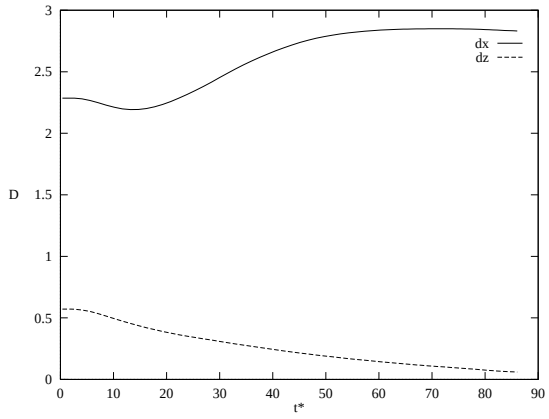

(c) Separation distance

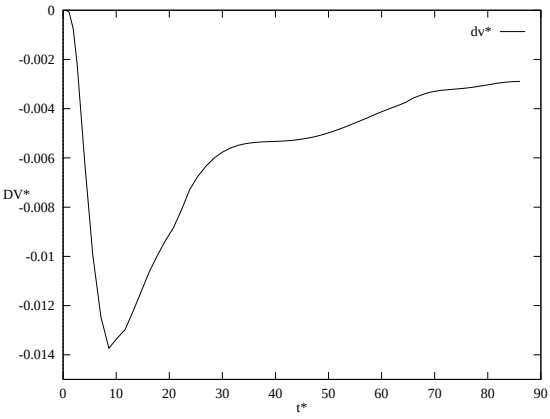

(d) Velocity difference

Figure 3.31: Quantitative description of the two-bubble interaction in Figures 3.28, 3.29 and 3.30. (a) Migration velocity versus time. (b) z component of the centroid of bubbles versus time. (c) The separation distance versus time and (d) The velocity difference versus time between the bubble on the right and the left. Velocity is scaled by reference velocity U_r, seperation distance and z axis by a, and time by a/U_r.

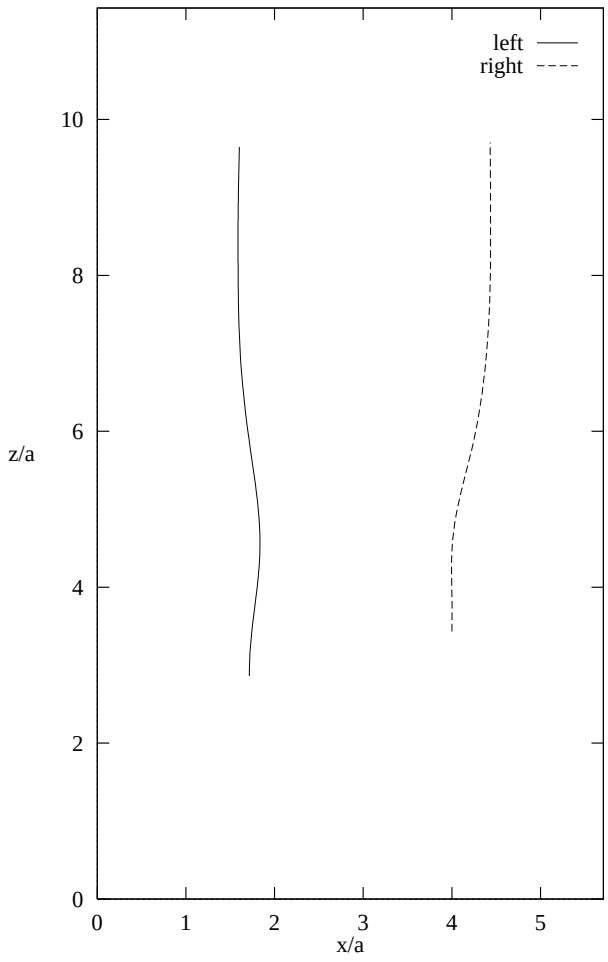

Figure 3.32: Trajectories of the center of mass of the bubbles. Both axis are scaled by the bubble radius a.

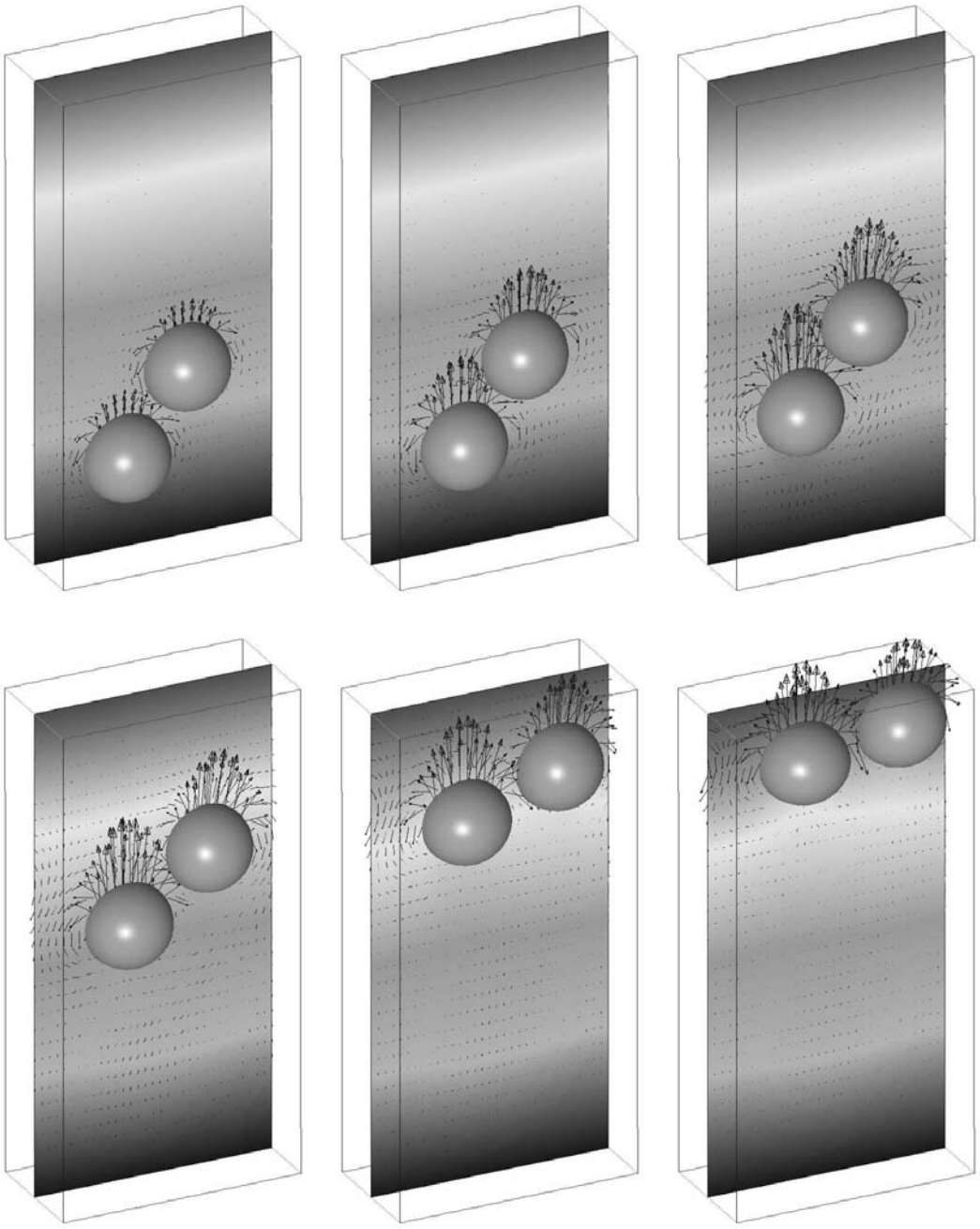

Figure 3.33: Velocity and temperature field for selected frames from the fully three-dimensional simulation of two-bubble interaction. The velocity field is shown at every other grid point in the middle plane of the computational box in y direction. Time progresses from left to right, top to bottom. The nondimensional time, t^*, is equal to $3.5, 7.0, 14.0, 35.0, 52.5, 63.0$. The nondimensional time is scaled by a/U_r and velocity is scaled by reference velocity, U_r. Computational domain size is $x/a = 5.71$, $y/a = 2.86$ and $z/a = 11.43$. Here, $Re = 60$, $Ma = 20$ and $Ca = 0.04166$.

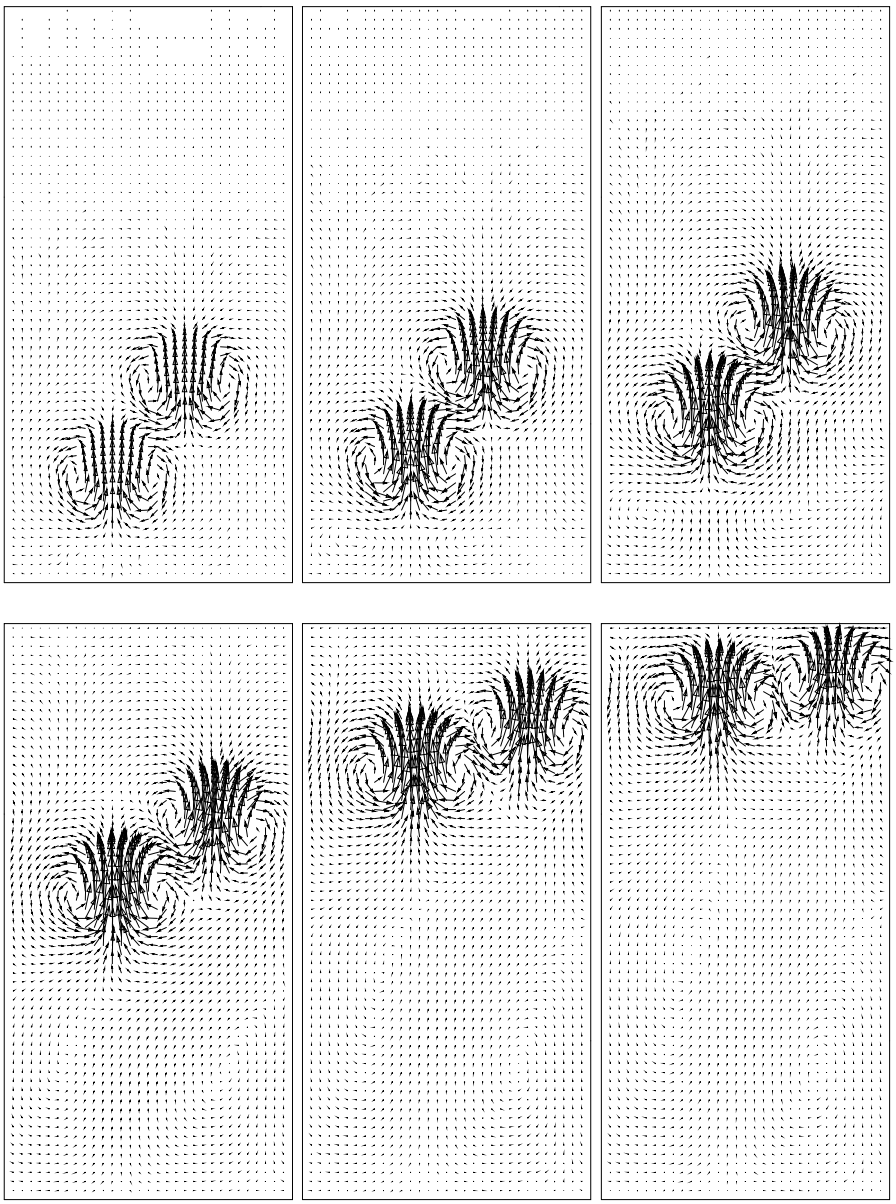

Figure 3.34: Velocity field for selected frames from the fully three dimensional computation of two bubble interaction. The velocity field is shown at every other grid point in the middle plane of the computational box in y direction. Time progresses from left to right. The nondimensional time, t^*, is equal to $3.5, 7.0, 14.0, 35.0,\ 52.5, 63.0$. The nondimensional time is scaled by a/U_r and velocity by U_r. Computational domain size is $x/a = 5.71$, $y/a = 2.86$ and $z/a = 11.43$.

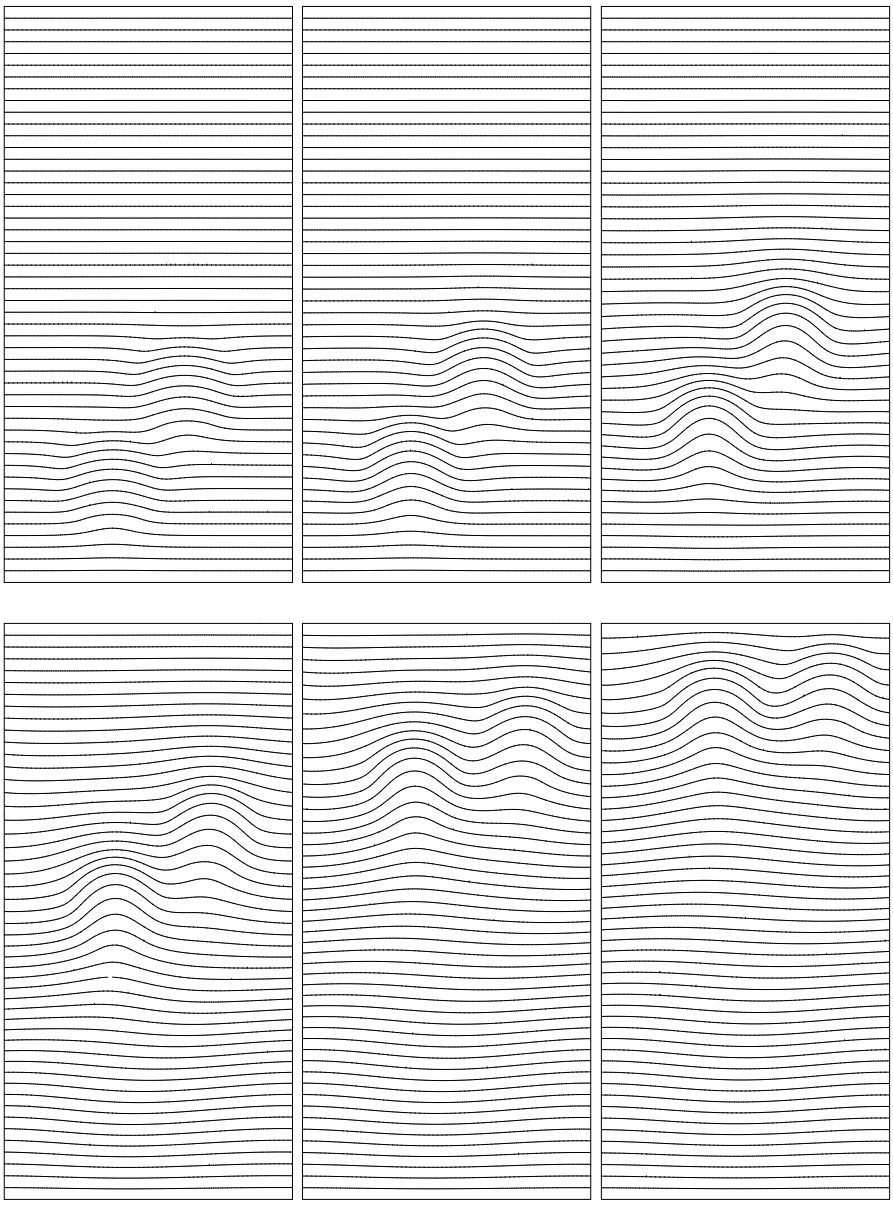

Figure 3.35: Temperature contours for selected frames from the fully three dimensional computation of two bubble interaction. 50 equally spaced contours are shown in the middle plane of the computational box in y direction. Time progresses from left to right. The nondimensional time, t^*, is equal to $3.5, 7.0, 14.0, 35.0, 52.5, 63.0$. The nondimensional time is scaled by a/U_r and temperature is scaled, after subtracting a reference temperature, by $a\nabla T_\infty$. Computational domain size is $x/a = 5.71$, $y/a = 2.86$ and $z/a = 11.43$.

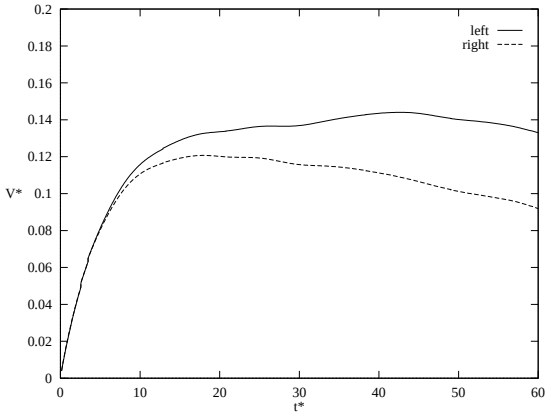

(a) Migration velocity

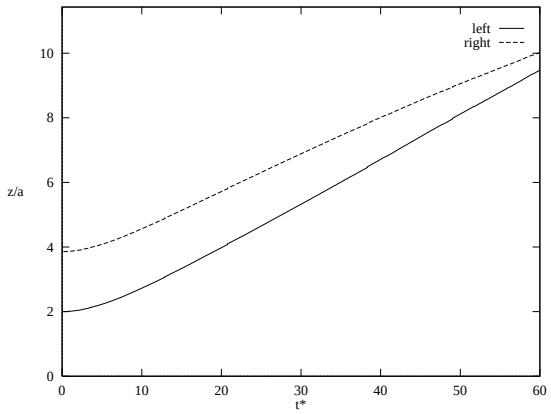

(b) Vertical position

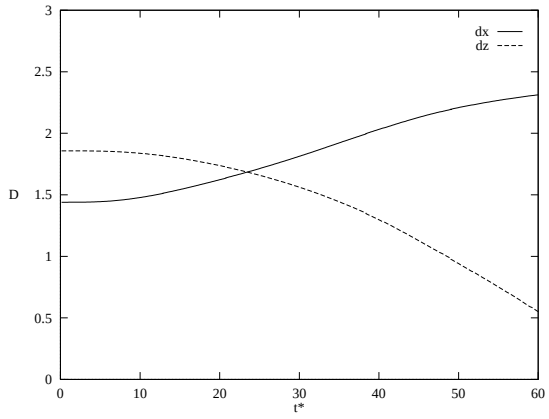

(c) Separation distance

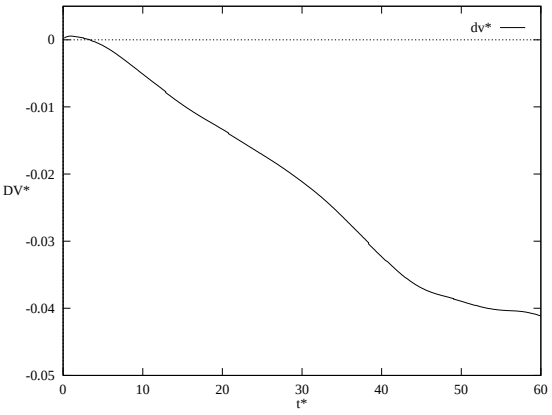

(d) Velocity difference

Figure 3.36: Quantitative description of the two-bubble interaction in Figures 3.33, 3.34 and 3.35. (a) Migration velocity versus time. (b) z component of the centroid of bubbles versus time. (c) The separation distance versus time and (d) The velocity difference versus time between the bubble on the right and the left. Velocity is scaled by reference velocity U_r, separation distance and z axis by a, and time by a/U_r.

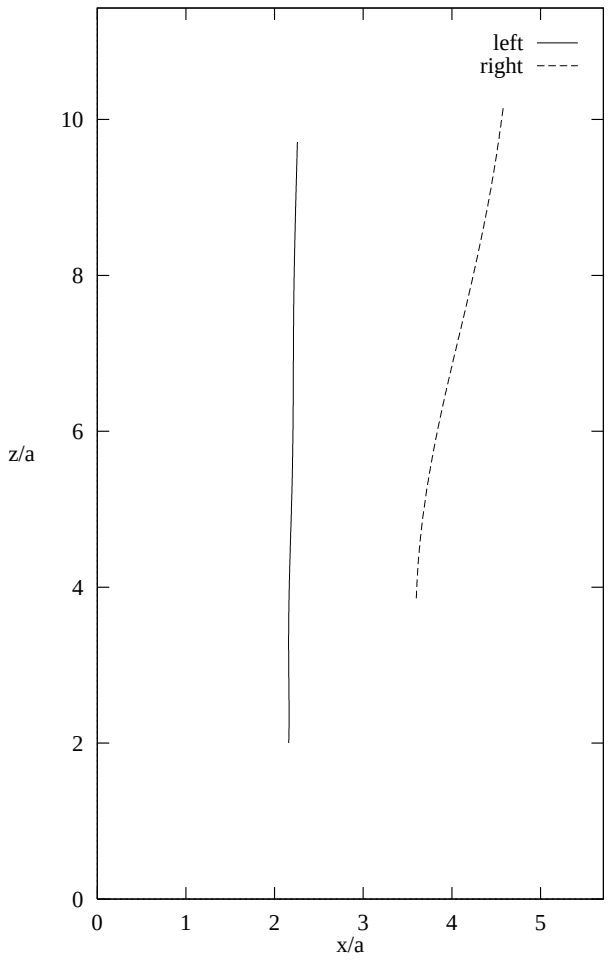

Figure 3.37: Trajectories of the center of mass of the bubbles. Both axis are scaled by the bubble radius a.

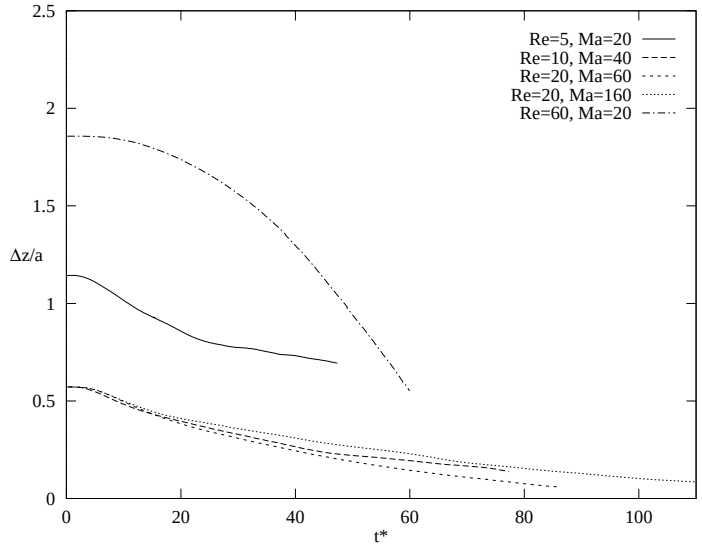

(a) The vertical separation distance

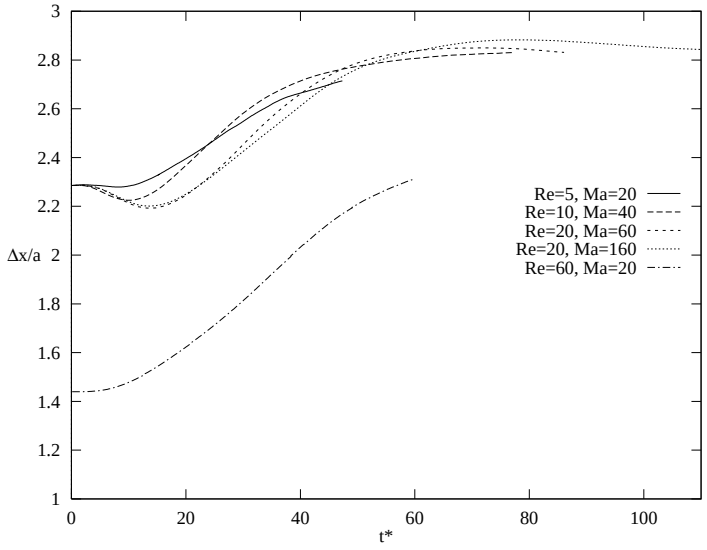

(b) The horizontal separation distance

Figure 3.38: Quantitative information for two-bubble interaction for different Reynolds and Marangoni numbers. (a) The vertical separation distance versus time. (b) The horizontal separation distance versus time. Time is scaled by a/U_r, separation difference, Δ, by, a. The differences are between the bubble on the right and the bubble on the left.